THE ASTROPHYSICAL JOURNAL, 504:636–660, 1998 September 10

WEAK LENSING ANALYSIS OF Cl 1358+62 USING *HUBBLE SPACE TELESCOPE* OBSERVATIONS[1]

HENK HOEKSTRA, MARIJN FRANX, AND KONRAD KUIJKEN
Kapteyn Astronomical Institute, University of Groningen, Postbus 800, 9700 AV Groningen, The Netherlands; hoekstra@astro.rug.nl, franx@astro.rug.nl, kuijken@astro.rug.nl

AND

GORDON SQUIRES
Center for Particle Astrophysics, University of California, Berkeley, CA 94720; squires@magicbean.berkeley.edu
Received 1997 October 23; accepted 1998 April 16

ABSTRACT

We report on the detection of weak gravitational lensing of faint, distant background objects by Cl 1358+62, a rich cluster of galaxies at a redshift of $z = 0.33$. The observations consist of a large, multicolor mosaic of *Hubble Space Telescope* WFPC2 images. The number density of approximately 50 background objects arcmin^{-2} allows us to do a detailed weak lensing analysis of this cluster. We detect a weak lensing signal out to ~ 1.5 Mpc from the cluster center. The observed distortion is consistent with a singular isothermal sphere model with a velocity dispersion of 780 ± 50 km s^{-1}. The total projected mass within a radius of 1 Mpc corresponding to this model is $(4.4 \pm 0.6) \times 10^{14}\ M_\odot$. The errors given here represent the random error due to the ellipticities of the background galaxies. The uncertainty in the redshift distribution introduces an additional systematic error of $\sim 10\%$ in the weak lensing mass. The weak lensing mass is slightly lower than dynamical estimates and agrees well with X-ray mass estimates. The mass distribution is elongated in a similar way as the light. The axis ratio of 0.30 ± 0.15 and position angle of $-21° \pm 7°$ were measured directly from the observations and agree very well with a previous strong lensing determination. A two-dimensional reconstruction of the cluster mass surface density shows that the peak of the mass distribution coincides with the peak of the light distribution. We find a value of $(90 \pm 13)h_{50}\ M_\odot\ L_{V\odot}^{-1}$ for the mass-to-light ratio, consistent with being constant with radius. The point-spread function of *HST* is highly anisotropic at the edges of the individual chips. This systematically perturbs the shapes of objects, and we present a method for applying the appropriate correction.

Subject headings: galaxies: clusters: individual (Cl 1358 + 62) — galaxies: fundamental parameters — gravitational lensing

1. INTRODUCTION

The technique of weak gravitational lensing has proven to be an important tool to study mass distributions in the universe. The projected mass distribution of foreground gravitational structures distorts the images of the faint background galaxies. As a result, gravitational lensing provides a direct measurement of the projected mass density (e.g., Kaiser & Squires 1993, hereafter KS).

Until recently, massive structures in the universe were studied through dynamical analyses of their luminous components. These studies have shown that large amounts of dark matter exist in the universe. For clusters of galaxies, a popular method uses the motions of the galaxies to estimate the mass, using the virial theorem. One also can estimate the cluster mass profile from X-ray observations when one assumes hydrostatic equilibrium and spherical symmetry (e.g., Allen & Fabian 1994).

Both methods assume some dynamical state or geometry in order to obtain the mass or a mass profile. The advantage of gravitational lensing is the fact that no such assumptions are needed. In the regime of weak gravitational lensing, one can calculate the projected mass surface density up to some additive constant from the observed distortion pattern (KS; Kaiser et al. 1995; Schneider & Seitz 1995; Schneider 1995; Squires & Kaiser 1996).

Since the first successful measurements of the weak gravitational distortions (Tyson, Valdes, & Wenk 1990), many massive clusters of galaxies have been studied (e.g., Bonnet, Mellier, & Fort 1994; Fahlman et al. 1994; Squires et al. 1996b; Luppino & Kaiser 1997, hereafter LK97). In principle, one can measure the gravitational distortion out to large radii from the cluster center, beyond the radii where X-ray observations or cluster kinematics can be used to determine the mass distribution.

So far, most weak lensing studies of clusters of galaxies have been undertaken using data from ground-based telescopes. These are affected by atmospheric seeing, which causes the images of the faint background galaxies to be enlarged and more circular.

In this paper we present the first weak lensing analysis of a cluster of galaxies using *Hubble Space Telescope* (*HST*) observations with a large field of view. Up to now, other weak lensing studies of clusters of galaxies with *HST* have been limited to cluster cores (Seitz et al. 1996; Smail et al. 1997). These observations consisted of single pointings and thus suffer from the limited field of view of *HST*.

Our data consist of a mosaic of 12 pointings, thus yielding a total field of view of approximately $8' \times 8'$. This combination of space-based observations and a large field of view provides an interesting opportunity to study the cluster Cl 1358+62 in great detail. The *HST* observations have also been used to study the evolution of cluster gal-

[1] Based on observations with the NASA ESA *Hubble Space Telescope* obtained at the Space Telescope Science Institute, which is operated by the Association of Universities for Research in Astronomy, Inc., under NASA contract NAS 5-26555

axies as a function of redshift (Kelson et al. 1997; van Dokkum et al. 1998).

Furthermore, the *HST* observations revealed a giant red arc approximately 21″ from the central galaxy. Franx et al. (1997) showed that the arc is a gravitationally lensed image of a galaxy at a redshift of 4.92. A strong lensing model based on this arc and its counterarc yields a velocity dispersion of 970 km s^{-1}, which is in fair agreement with the cluster kinematics (Franx et al. 1997).

An advantage of *HST* observations is the high number density of galaxies one can reach in relatively short exposures. Previous *HST* studies have routinely achieved $\simeq 100$ galaxies $arcmin^{-2}$ (e.g., Seitz et al. 1996; Smail et al. 1997). With only 3600 s exposures per pointing, we obtain a number density of ~ 50 useful background galaxies $arcmin^{-2}$ in both F606W and F814W.

Another important advantage of *HST* over ground-based observations is the size of the point-spread function (PSF). Most of the faint objects are small. To recover the lensing signal, one needs to correct for the effect of seeing (Bonnet & Mellier 1995; Kaiser, Squires, & Broadhurst 1995a, hereafter KSB95; LK97; Fischer & Tyson 1997). For objects with sizes comparable to the PSF, these corrections become very large, amplifying the uncertainty in the ellipticity due to photon noise. As a result the scatter in the derived ellipticities of the galaxies is larger than the expected scatter due to their intrinsic shapes. Consequently, for a given number density of background objects, the accuracy of weak lensing studies based on *HST* observations will be higher than the results from ground-based data.

We will investigate the dark matter and galaxy distribution in the cluster of galaxies Cl 1358+62. The cluster is at a redshift of 0.33 with measured velocity dispersions of 1027^{+51}_{-45} km s^{-1} (Fisher et al. 1998) and 910 ± 54 km s^{-1} (Carlberg, Yee, & Ellingson 1997). It is also a rich cluster at its redshift, with Abell richness class 4 (Luppino et al. 1991). The cluster has a strong binary nature (Carlberg et al. 1997) with a massive substructure moving at ~ 1000 km s^{-1} with respect to the cluster center. This substructure is outside the region observed in this paper. Cl 1358 has a measured X-ray luminosity of $L_X(0.2\text{–}4.5\ \mathrm{keV}) = 7 \times 10^{44}\ h_{50}^{-2}$ ergs s^{-1} (Bautz et al. 1997), which makes it a luminous cluster in X-ray.[2]

The observations and data reduction are briefly outlined in § 2. In § 3 we discuss the method we used, including the corrections for both the anisotropy and the size of the PSF and the camera distortion. The object selection for the weak lensing analysis is described in § 4. The light distribution is discussed in § 5. The redshift distribution we used to calculate the critical surface density is presented in § 6. The results from the weak lensing analysis are presented in § 7. In the Appendices we address the issue of PSF and camera distortion corrections.

2. DATA

The cluster Cl 1358+62 was observed with the WFPC2 camera on board the *HST* in 1996 February. The observations consist of 12 pointings of the telescope. Each pointing consists of three exposures of 1200 s in both the F606W and F814W filter. Combining the observations yields a mosaic of approximately 8′ × 8′, which ranks it among the largest fields observed with *HST*. The total area covered by the observations is approximately 53 $arcmin^2$.

The data reduction is described in van Dokkum et al. (1998). For the weak lensing analysis we omit the data of the PC chips because of the brighter isophotal limit.

3. METHOD

Our analysis technique is based on that developed by KSB95, with a number of important modifications. We summarize the method here in order to highlight the differences, which center on the correction of certain arithmetic errors in KSB95's formulae and on a careful study of the effect of the weight function used in calculating image moments. The details of the complete method are given in the Appendices.

The first step in the analysis is to detect the faint galaxy images, which we do with the KSB95 algorithm and software. The shapes of these objects are then quantified by calculating the central second moments I_{ij} of the image fluxes and forming the two-component polarization

$$e_1 = \frac{I_{11} - I_{22}}{I_{11} + I_{22}} \quad \text{and} \quad e_2 = \frac{2I_{12}}{I_{11} + I_{22}} \tag{1}$$

(Blandford et al. 1991).

Because of photon noise, unweighted second moments cannot be used. Instead, we use a circular Gaussian weight function with dispersion r_g equal to the radius of maximum significance given by the KSB95 detection algorithm.

Before we can search for lensing-induced systematics in the shapes of the objects we have detected, other sources of distortion have to be corrected for. The relevant one for *HST* observations is smearing by the PSF, which may be viewed as two separate effects: the effect of the anisotropy of the WFPC2 PSF (see below), which will cause a systematic polarization of galaxy images, and the circularization of the galaxy images through convolution with the isotropic part.

We investigated the PSF of WFPC2 using stars from our observations. Using these stars we found indications of a significant anisotropy in the PSF. The results are shown in Figure 1. The orientation of the sticks indicates the direction of the major axis of the stars, and the size is proportional to the size of the anisotropy.

Figure 1 clearly shows that the anisotropy changes as a function of position and becomes larger toward the edges of the chips. Unfortunately, the limited number of stars in our observations does not provide sufficient coverage of the chips. One also finds from this figure that the patterns in the two filters are fairly similar.

To investigate the PSF anisotropy as a function of position in more detail, we retrieved observations of the globular cluster M4 (Richer et al. 1997) from the *HST* archive. The data consist of a pointing at the core and two pointings at one effective radius. The polarization pattern we measured from isolated stars in this globular cluster is shown in Figure 2.

Figure 2 shows that especially at the edges of the chips the anisotropies are large. According to Holtzman et al. (1995a), the PSF changes with field position because of a variable pupil function and small aberrations. The anisotropy introduced by the camera distortion is discussed below. Also, variations in time occur because of jitter and

[2] Throughout this paper we will use $h_{50} = H_0/(50\ \mathrm{km\ s^{-1}\ Mpc^{-1}})$, $q_0 = 0.5$, and $\Lambda = 0$. This gives a scale of $1'' = 5.8\ h_{50}^{-1}$ kpc at the distance of Cl 1358.

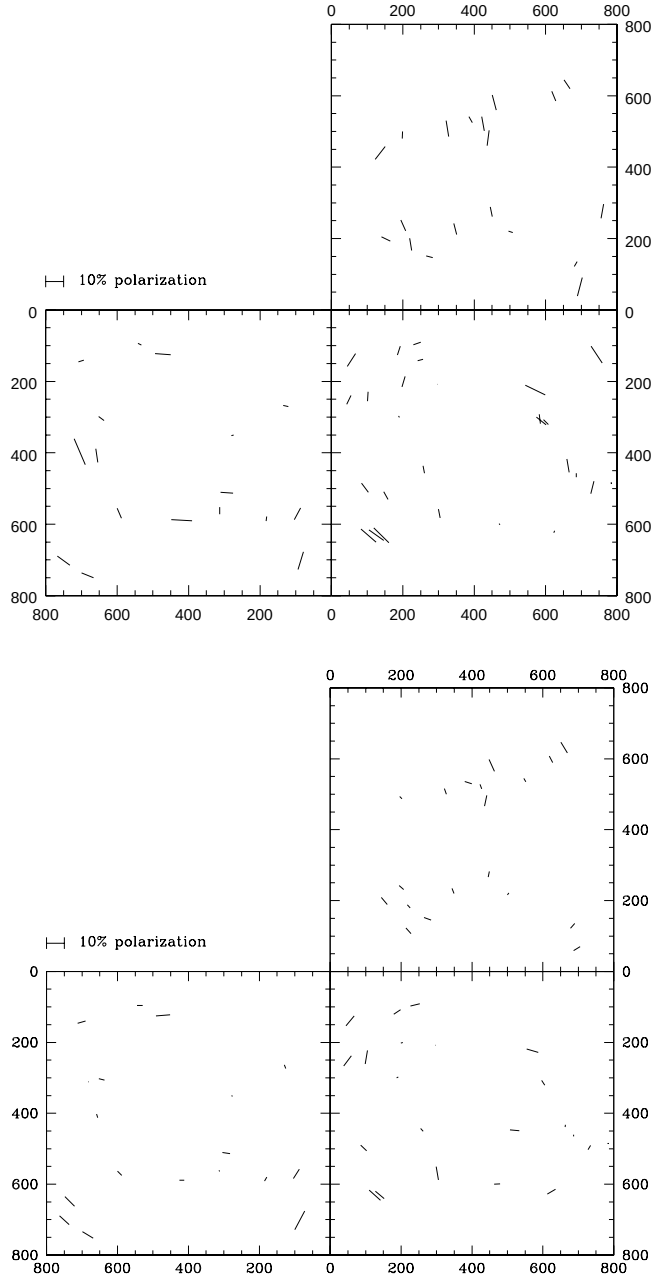

FIG. 1.—Polarization field of stars taken from observations of the cluster of galaxies Cl 1358+62. The orientation of the sticks shows the direction of the major axis of the PSF, whereas the length is proportional to the size of the anisotropy. The polarizations are calculated using a Gaussian weight function with a dispersion of 1 pixel, which is the value found by the peak finder. The upper figure shows the results from the F606W data. The lower figure shows the results from the F814W data. The lower left panel is chip 2, lower right is chip 3, and the upper right one denotes chip 4. We have omitted chip 1, which is the planetary camera.

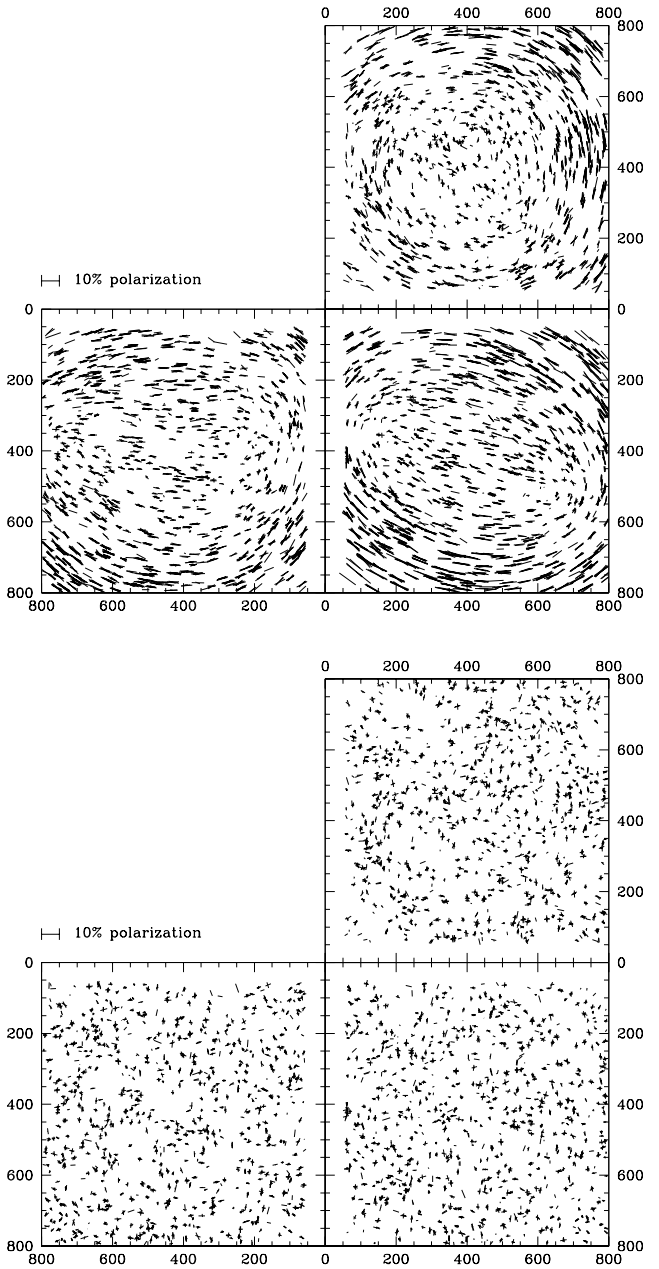

FIG. 2.—*Upper panel*: polarization field of stars taken from observations of the globular cluster M4. The orientation of the sticks shows the direction of the major axis of the PSF, whereas the length is proportional to the size of the anisotropy. These observations were taken in the F814W filter. The polarizations are calculated using a Gaussian weight function with a dispersion 1 pixel, which is the value given by the peak finder. The lower left panel is chip 2, lower right is chip 3, and the upper right one denotes chip 4. We have omitted chip 1, which is the planetary camera. *Lower panel*: Residuals after subtracting a third-order polynomial fit for each polarization component (10 parameters for each component).

focus changes. Nevertheless, we use the M4 data as a starting point for the PSF modeling and correct for residual differences as described below.

In the original KSB95 approach, only one size weight function was used for the anisotropy model. This is generally sufficient for ground-based data, for which the PSF can be well represented by a Gaussian. We have found that the very non-Gaussian WFPC2 PSF requires that we use correction parameters that depend on the size of the object we want to correct. We fitted a third-order polynomial to the polarization field of the globular cluster for a given width r_g of the weight function. This yields a series of maps of the PSF anisotropy as a function of r_g, which we will use to correct the measured galaxy image shapes.

The residuals after subtracting the model from the data (using a weight function with a dispersion of 1 pixel) are shown in the lower panel of Figure 2. In this figure no systematic patterns are seen, and a higher order fit provided no significant improvement.

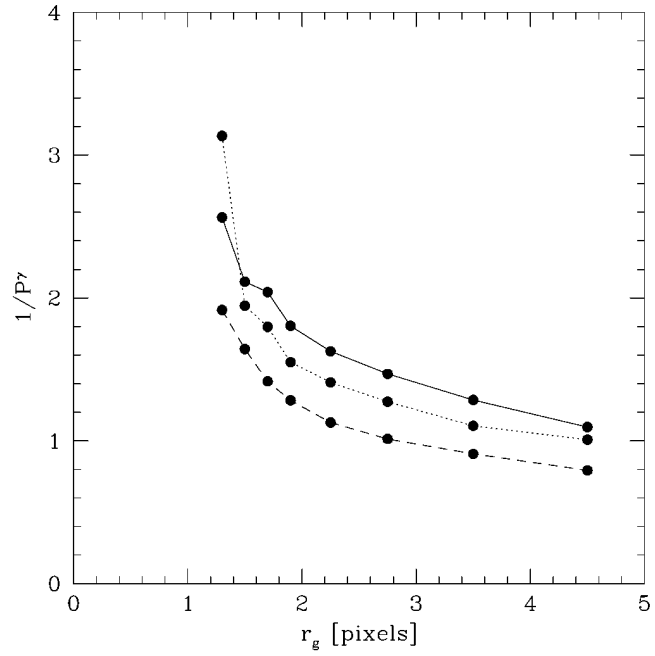

FIG. 3.—Correction factor when one goes from polarization to distortion as a function of the radius of maximum significance for the F814W data. The solid line shows the results for objects with 18 < F814W < 22, the dotted line for objects with 22 < F814W < 24, and the dashed line for objects with 24 < F814W < 26.5. This correction factor is the inverse of the "preseeing" shear polarizability.

Because the PSF can change with time, it is important to know how stable the pattern shown in Figure 2 is. To investigate this we retrieved archival *HST* data for another globular cluster (NGC 6752) in the F814W band and compared the results found for that cluster to the results found for M4. We also compared the results from M4 to the measurements of the stars in the mosaic. In both cases we found a fair agreement, although some systematic deviations from the model are seen. These deviations are on the few percent level.

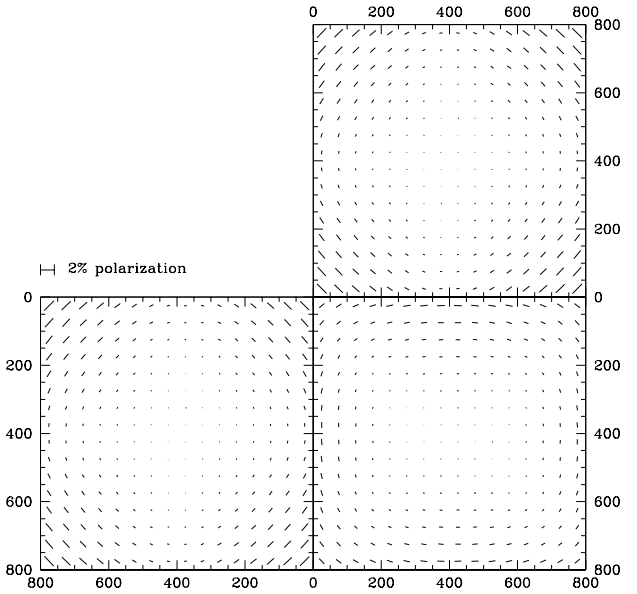

FIG. 4.—Shear introduced by the WFPC camera distortion. The shear was calculated using the coefficients for the distortion given in Holtzman et al. (1995a). The orientation of the sticks shows the direction of the shear, and the length is proportional to the size. The lower left panel is chip 2, lower right is chip 3, and the upper right one denotes chip 4. We have omitted chip 1, which is the planetary camera.

To correct for these systematic differences between the observations of M4 and our mosaic, one can fit a low-order polynomial to the residuals between the model and the mosaic. Because of the low number of stars per individual pointing, we stack the results of all 12 pointings for each individual chip. We found that for our observations a zeroth order polynomial of $\leq 1\%$ is sufficient. We then repeat the procedure for different choices of the weight function radius r_g, finally ending up with maps at a number of values of r_g of the PSF polarizations and polarizabilities for the three wide-field chips.

The effect of an anisotropic PSF on the polarization e_α of a galaxy image is quantified by the "smear polarizability," $P^{\rm sm}$, which measures the response of the image polarization e_α to a convolution with a small anisotropic kernel. The value of $P^{\rm sm}$ can be estimated for each observed image and also depends on the weight function used in calculating e_α. In the Appendices, we correct a small analytical error in the expression for $P^{\rm sm}$ given by KSB95. Correcting the observed galaxy polarizations using

$$e_\alpha \rightarrow e_\alpha - \sum_\beta \frac{P^{\rm sm}_{\alpha\beta}}{P^{\rm sm*}_{\beta\beta}} e^*_\beta \,, \qquad (2)$$

where the asterisks refer to parameters measured for stellar images, then undoes the effect of PSF anisotropy. In our analysis we take care to use the same radius for the Gaussian weight function for all parameters in this equation, although it may differ from galaxy to galaxy—unlike KSB95, who use a smaller r_g for the stars than for the galaxies. This turns out to be significant for the WFPC2 PSF, as we justify and discuss in the Appendices. In practice, we interpolate the map of stellar polarizations and polarizabilities to r_g equal to each galaxy's radius of maximum significance.

The next step is to deduce the distortion from the anisotropy-corrected galaxy polarizations. Both the (now effectively isotropic) PSF and the circular weight function tend to make objects rounder. These effects may be corrected for using the "preseeing shear polarizability" P^γ of LK97. This quantity can again be estimated from the observed galaxy and star images (in the Appendices we correct a small analytical error in the expression for the shear polarizability in KSB95), and again we have found that it is important to use the same value of r_g for star and galaxy polarizations and polarizabilities when constructing P^γ, as discussed further in the Appendices.

Because of the noisiness of individual estimates for P^γ, we determine the mean P^γ for a series of bins of magnitude and r_g. These mean values are used to estimate the distortion. In Figure 3 we show the correction factor when going from a polarization to a distortion as a function of the radius of maximum significance and brightness of the object. The correction converges to a value of ~ 1 for large objects. The smallest objects have a correction factor that is twice as large. For ground-based data much higher values would be found. Figure 3 also shows that the correction factor increases with increasing brightness, indicating that these objects have on average different profiles than fainter

objects. Using the original equations from KSB95 would underestimate the shear polarizability by approximately 13%, therefore overestimating the distortion by a similar amount.

We finally estimate the distortion g at a certain position using

$$g_\alpha = \frac{\langle e_\alpha \rangle}{\langle P^\gamma_{\alpha\alpha} \rangle}. \quad (3)$$

So far we have neglected the effect of the camera distortion. A distortion introduced by the camera mimics a shear. We show in Appendix A2 that the correction for this effect is straightforward. To obtain the true shear one simply has to subtract the camera shear from the observed shear in equation (3).

The distortion of WFPC2 is described in Holtzman et al. (1995a). We used the coefficients from their paper to calculate the shear induced by the camera distortion. The resulting shear field is presented in Figure 4. The effect is small; the largest values are 2% in the corners of the chips. This shear field is used to correct the observed distortion.

The *HST* PSF is badly sampled. As a result it introduces some extra scatter in the measurement of e_1. To investigate how the correction scheme is affected by the sampling problem, we used simulations, which are described in the Appendices. The simulations show that the corrections can be applied safely to objects that have a radius of maximum significance of 1.2 pixels and larger.

4. OBJECT SELECTION

The cluster was observed in two filters: F606W and F814W. For each pointing and filter, we detected objects with a significance of 4 σ over the local sky, using the peak finder described in KSB95. Only objects that were detected in both the F606W and F814W exposure were used for further analysis. Although it provides an efficient way to remove spurious detection, a disadvantage of this approach is that it also removes faint red objects (only detected in F814W) and faint blue objects (only detected in F606W). Objects that were detected both in F606W and F814W but clearly did not match in size were also removed.

We convert the measured counts to F606W and F814W magnitudes, zero-pointed to Vega, using the conversions given in Holtzman et al. (1995b). We add 0.05 magnitude to the zero points to account for the charge transfer efficiency effect. Figure 5 shows a plot of the magnitude of objects versus the calculated half-light radius. Stars are located in the vertical locus in this plot. Bright stars saturate, and their measured sizes increase. This figure shows that one can separate moderately bright stars from galaxies and saturated stars. The stars we identified this way were used to examine the PSF anisotropy (see Fig. 1).

We select objects with half-light radii 1.2 times the half-light radii from the PSF as galaxies. From this sample we removed objects with r_g less than 1.2 pixels, as we can correct only galaxies that have a radius of maximum significance of 1.2 pixels or more reliably. This is demonstrated in the Appendices.

This yields a catalog of 4175 objects corresponding to a number density of 79 galaxies arcmin^{-2}. Because of our selection criteria, the total number of detected galaxies is slightly higher.

Combining the F606W and F814W observations, we determined the colors of galaxies in our catalog. The resulting color-magnitude diagram is shown in Figure 6. This figure clearly shows the sharp color-magnitude relation of Cl 1358, which is discussed in van Dokkum et al. (1998).

The sharp cluster color-magnitude relation allows us to remove many bright cluster members from our catalog. At the faint end the cluster sequence becomes broader and

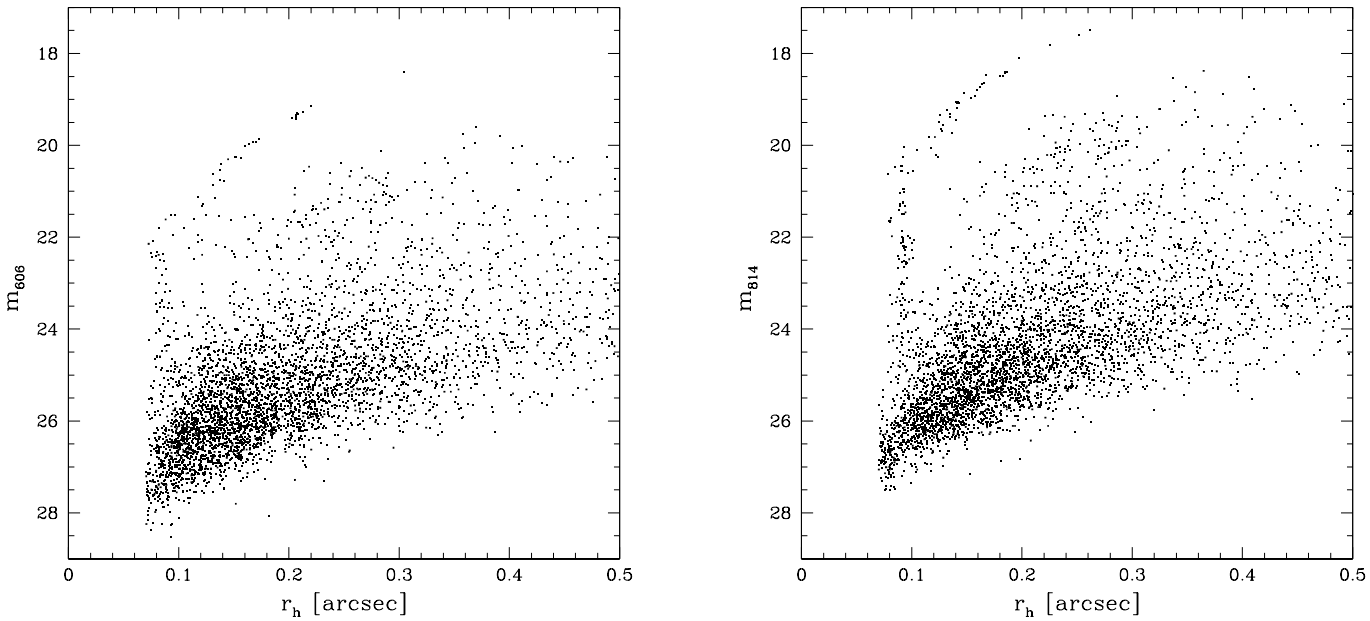

FIG. 5.—Plots of the magnitude of selected objects vs. the calculated half-light radius. The left plot shows the results for the F606W data. The right plot shows the results of the F814W data. In both figures the vertical stellar locus is clearly seen. We identify galaxies as objects that have a half-light radius that is 1.2 times that of the stars.

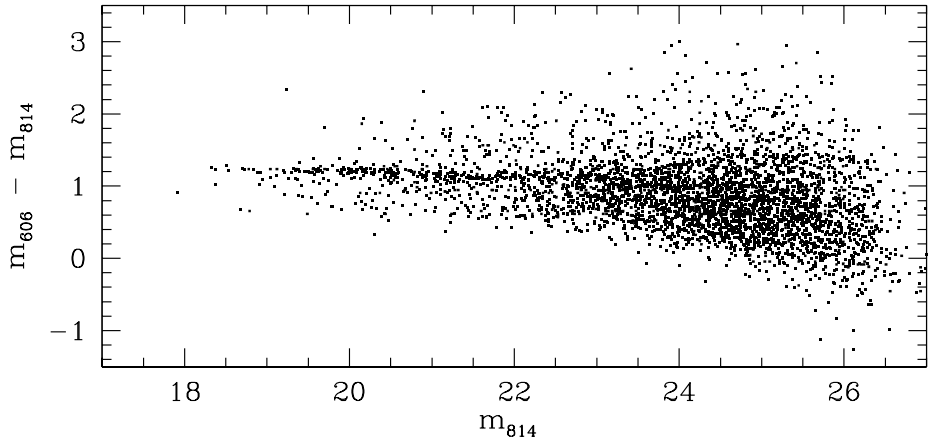

FIG. 6.—Color-magnitude diagram for objects detected both in F606W and F814W. In this figure all 4175 objects we identified as being galaxies are plotted. Also, notice the very sharp cluster color-magnitude relation.

blends with the population of background galaxies. The color information allows us to create color-selected subsamples of background galaxies. The subsamples we use in the weak lensing analysis are listed in Table 1.

5. LIGHT DISTRIBUTION

We calculated the luminosity in the redshifted V band as described in van Dokkum et al. (1998). The direct transformation from the *HST* filters to the redshifted V band is given by

$$V_z = m_{814} + 0.2(m_{606} - m_{814}) + 0.65 ,$$

where V_z denotes the redshifted V band magnitude. The luminosity in the redshifted V band is

$$L_V = 10^{0.4(M_{V\odot} - V_z + DM + A_{\rm F814W})} L_{V\odot} ,$$

where $M_{V\odot} = 4.83$ is the solar absolute V magnitude, DM is the distance modulus, and $A_{\rm F814W}$ is the extinction correction in the F814W band. The redshift of 0.33 gives a distance modulus for Cl 1358 of $41.63 - 5 \log h_{50}$ (or $41.52 - 5 \log h_{50}$ using $q_0 = 0.1$). Taking galactic extinctions from Burstein & Heiles (1982) and using the results from Cardelli, Clayton, & Mathis (1989), we find a value of 0.02 for $A_{\rm F814W}$.

To measure the total luminosity of the cluster galaxies, we measured aperture magnitudes using apertures with 3″ diameter. Confirmed cluster galaxies were fitted by exp $(r^{1/n})$ profiles by van Dokkum (1998). Using the total magnitudes inferred from these fits, we estimate the aperture correction as a function of aperture magnitude.

Many galaxies in the Cl 1358 field were observed spectroscopically (Fisher et al. 1998). Down to $V_z = 20.5$ the catalog of confirmed cluster members is complete. To estimate the light of the cluster galaxies we use the confirmed cluster galaxies if they are brighter than $V_z = 20.5$ (F814W $\approx$ 19.6). For galaxies with $20.5 < V_z < 22.5$, we select galaxies that lie on or less than 0.2 magnitude below the color-magnitude relation, yielding a catalog that contains 341 galaxies. At even fainter magnitudes the color-magnitude relation blends with the population of background galaxies.

TABLE 1

PROPERTIES OF THE VARIOUS SUBSAMPLES TAKEN FROM THE FINAL CATALOG OF GALAXIES

Name	m_{814}	$m_{606} - m_{814}$	Number of Galaxies	$\bar{n}$
Bright.....	22–25	∉[0.9, 1.5]	1272	24
Faint.....	25–26.5	...	1392	26
Blue.....	22–26.5	<0.9	1835	35
Red	22–26.5	>1.5	393	7

To obtain a qualitative description of the cluster light distribution, we calculated both the galaxy number density and the galaxy light. Gray-scale plots of the luminosity and number-weighted light distributions of the sample of bright cluster galaxies are presented in Figure 7. Both distributions have been smoothed with a Gaussian filter with scale 0.′4. The galaxy number density and the luminosity weighted distributions of the cluster sample look quite similar. The dominant structure in both distributions coincides with the region around the central galaxy in the cluster. Both figures show that the cluster light is elongated north-south. Several other concentrations are also visible. Of these, the one to the north is the most significant. The extension to the south and the concentration to the north were already reported in Luppino et al. (1991).

To investigate the clustering of background galaxies, we also show the number density distribution of all detected galaxies. We split the sample into two bins. Figure 7*c* shows the number density distribution of galaxies with F814W brighter than 22.5; Figure 7*d* shows the result for galaxies fainter than F814W magnitude 22.5.

The counts in the bright sample are dominated by the cluster. For the faint galaxies we see two peaks near the edges of the observed region. Because these enhancements in the number density are not seen in the bright sample, they correspond to galaxy concentrations at redshifts higher than the redshift of Cl 1358.

Using the sample of bright cluster galaxies, we estimate a luminosity function. We found that a Schechter function with $\alpha = -1.1$ and $L_* = 4.5 \times 10^{10} L_{V\odot}$ fits the observed counts well. From this luminosity function we estimate that galaxies fainter than $V_z = 22.5$ contribute 11% to the total light of the cluster.

We calculate the cumulative light profile from the sample of bright cluster galaxies. The profile is multiplied by a factor of 1.11 to account for the light from faint cluster galaxies. The cumulative light profile is shown in Figure 8. The solid line in this figure corresponds to an isothermal

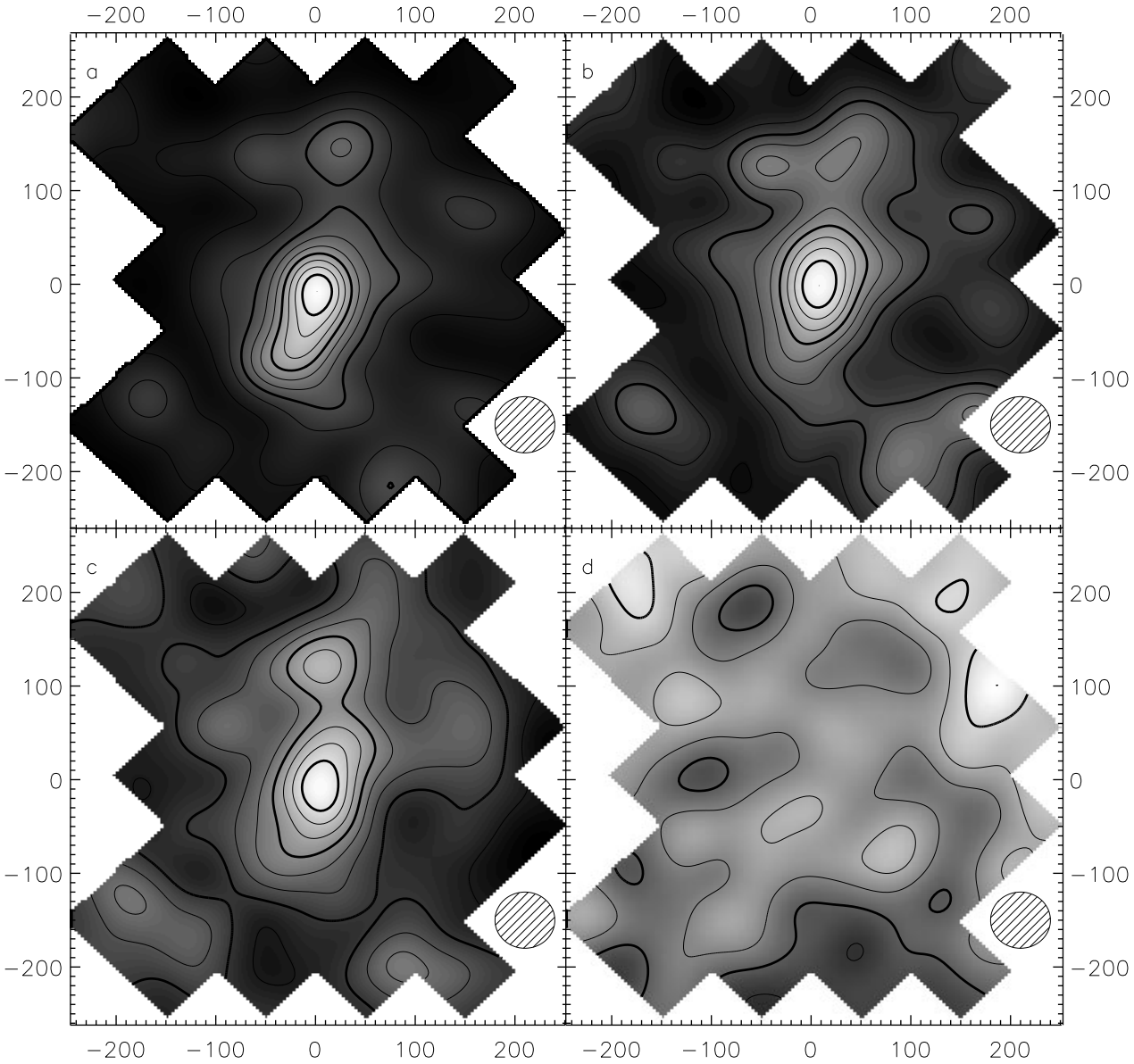

FIG. 7.—(*a*) Luminosity-weighted distribution of cluster galaxies brighter than V_z of 22.5 magnitude; (*b*) number density distribution of this sample of cluster galaxies; (*c*) number density distribution of all detected galaxies brighter than $F814W$ 22.5; and (*d*) number density distribution of all detected galaxies fainter than $F814W$ 22.5. The distributions have been smoothed with a Gaussian filter with scale 0.4; the shaded circle indicates the FWHM of the smoothing function. The contours are 10%, 20%, and so on, of the peak value. The total size of the image is $500'' \times 530''$, within which the mosaic covers the indicated region. The orientation is such that north is up and east is to the left.

profile, indicating that the radial light profile is close to isothermal. The total luminosity within an aperture of 1 Mpc is $(5.19 \pm 0.26) \times 10^{12} L_{V\odot}$.

6. REDSHIFT DISTRIBUTIONS

From the measured distortion one can calculate the dimensionless surface density κ (e.g., Schneider, Ehlers, & Falco 1992) up to some additive constant. To convert this dimensionless surface density into a physical surface density, we have to estimate a mean critical surface density

$$\Sigma_{\rm crit} = c^2 (4\pi G D_l \beta)^{-1} ,$$

where D_l is the angular diameter distance to the lens, and

$$\beta = \left\langle \max \left[0, 1 - \frac{1 - (1 + z_l)^{-1/2}}{1 - (1 + z_s)^{-1/2}} \right] \right\rangle$$

in an Einstein-De Sitter universe ($\Omega_0 = 1$) when z_l and z_s are the redshifts of lens and source, respectively. The value of β depends on the redshift distribution of the background galaxies. The redshift of Cl 1358 gives an angular diameter distance of 1.20 h_{50}^{-1} Gpc, yielding a value of $\Sigma_{\rm crit} = 1380 \beta^{-1}\ h_{50}\ M_\odot\ {\rm pc}^{-2}$ (using $q_0 = 0.1$, the angular diameter distance to Cl 1358 is 1.14 h_{50}^{-1} Gpc).

Unfortunately, the redshift distribution of the faint galaxies that are used in this weak lensing analysis is uncertain. Down to a magnitude of $I \sim 23$, spectroscopic redshift surveys give a fairly good picture of the redshift distribution. At fainter magnitudes redshifts can be estimated by broadband photometric redshift techniques (e.g., Sawicki, Lin, & Yee 1997; Lanzetta, Yahil, & Fernández-Soto 1996; Lanzetta, Fernández-Soto, & Yahil 1997), although the reliability of these techniques is still uncertain.

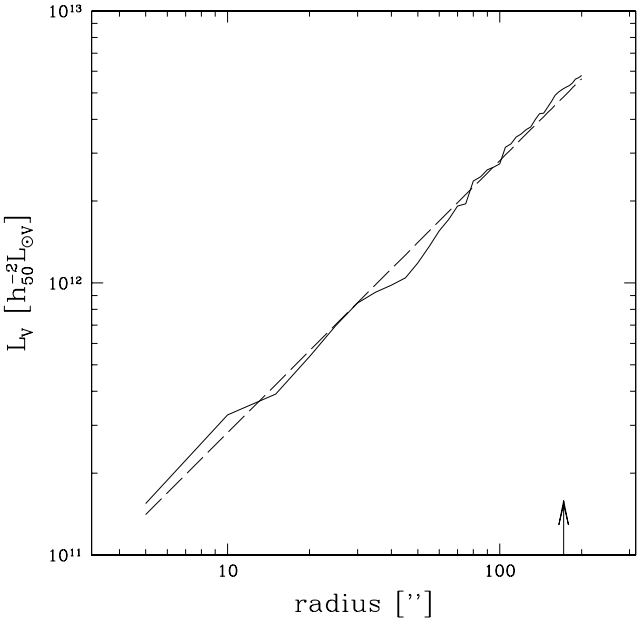

FIG. 8.—Cumulated, passband-corrected, L_V luminosity as a function of radius from the central elliptical galaxy. The dashed line corresponds to a isothermal profile. The arrow indicates a radius of 1 h_{50}^{-1} Mpc.

Another approach is to model galaxy evolution and estimate redshift distributions from the model predictions. The results are uncertain and the distributions at faint magnitudes can differ much among various models.

We used $n(m, z)$ distributions provided by Gronwall & Koo (1995), Bouwens & Silk (1996), Bouwens, Broadhurst, & Silk (1998), and Babul & Ferguson (1996) to estimate β for our galaxy samples. The Gronwall-Koo model and the Babul-Ferguson model we have were calculated for a flat universe. The low-Ω Pozzetti model (Pozzetti, Bruzual, & Zamorani 1996) was calculated by Bouwens et al. (1997).

If available, we used low-Ω models, because our results (see § 7.3) are consistent with a low-density universe. Because of the relatively low redshift of Cl 1358 and the relatively high redshifts of the background galaxies, the value for β does not change whether one uses $q_0 = 0.5$ or $q_0 = 0.1$.

Another problem arises for the faint sample because of the size cut that was needed to get reliable corrections for the PSF effects. Such a size cut will change the redshift distribution of the objects in our faint sample and therefore increase the uncertainty in β. The effect of the size cut is negligible for the bright galaxies. For the Gronwall-Koo model, we estimated the effect of the size cut, assuming that the missing galaxies are those with the highest redshifts. This procedure gives an indication of the uncertainty in β due to the size cut. A similar procedure did not change the β values of the Pozzetti model.

TABLE 2

THE MEAN VALUE FOR β FOR THE VARIOUS SUBSAMPLES

Name	GK	GK1	LYF	BF	POZ	Used
Bright	0.53	0.55	0.60	0.67	0.65	0.62
Faint	0.63	0.58	0.64	0.58	0.69	0.62
Bright + faint...	0.58	0.57	0.62	0.62	0.68	0.62
Blue	0.58	0.57	0.62	0.63	0.67	0.62
Red	0.55	0.55	0.61	0.65	0.66	0.62
Blue + red	0.58	0.56	0.61	0.63	0.67	0.62

NOTE.—Values are given using GK for the Gronwall-Koo (1995) model, GK1 for the Gronwall-Koo model with estimated effect of size cut at the faint end, LYF for photometric redshifts from Lanzetta et al. (1996), BF for the Babul-Ferguson (1996) model, and POZ for the Pozzetti et al. (1996) model. In the last column we give the value we use in this paper.

The distributions we used did not contain color information. Therefore we do not know the real redshift distributions for the blue and red sample, but we will assume that they are comparable.

Another problem is cluster member contamination, which will lower the lensing signal (or, equivalently, lower β). For bright galaxies, the cluster color-magnitude relation is fairly well defined (see Fig. 6), although there will be some bright cluster galaxies that are blue. At the faint end, the color-magnitude relation becomes broader toward the blue, which makes a color selection less effective. Cluster member contamination will be worst near the center of the cluster, because there the number density of cluster members is highest and the statistics are poor. Selecting galaxies based on their colors allows one to lessen the effect of contamination. The effect of cluster member contamination on our measurements is discussed in § 7.1.

Gravitational lensing not only changes the shapes of the background galaxies, it also magnifies them. As a result the measured flux is increased. Because of this magnification bias, the mean redshift of galaxies in a certain magnitude bin is a function of distance to the center of the cluster (assuming a circular mass distribution), and therefore β and the critical surface density are also functions of distance to the center. Although the effect is fairly small for this cluster, for more massive clusters β may change significantly with radius (e.g., Fischer & Tyson 1997).

In Table 2 we list values for β for the various subsamples and redshift distributions. By comparing the various values for β, one gets an idea of the uncertainty in β. Because of the relatively low redshift of Cl 1358, the agreement between the various distributions is fairly good. The uncertainty in the mass estimate due to the uncertainty in the redshifts of the background sources is $\sim$10%. We will use a value of $\beta = 0.62$ in this paper. The uncertainty in β is systematic and will hopefully decrease in the future. We therefore do not include the uncertainty in β in the error budget of the weak lensing analysis.

Because the critical surface density depends on the source redshift distribution, the observed distortion for samples with different redshift distributions reflects this difference. Therefore, by comparing the distortion for different samples of background sources, one can in principle constrain possible redshift distributions. We fitted an singular isothermal model [$\kappa(r) = \kappa_0/r$, where r is in arcseconds] to the observations of the bright and faint sample for radii larger than 40″. For the bright sample we find $\kappa_0 = 5.5 \pm 1.0$ and for the faint sample $\kappa_0 = 4.3 \pm 1.0$, yielding a ratio of 1.3 ± 0.4 for $\beta_{\rm bright}/\beta_{\rm faint}$. The error bars are calculated from the errors in the tangential distortion. This result does not rule out any of the distributions discussed above.

7. WEAK LENSING RESULTS

7.1. *Mass Estimate*

From the observations one can measure only the distortion g, which is related to the shear γ through $g = \gamma/(1 - \kappa)$. In the weak lensing limit ($\kappa \ll 1$) the distortion is equal to the shear.

To examine the mass distribution of Cl 1358, we first examine the tangential distortion, g_T, which is defined as $g_T = -(g_1 \cos 2\phi + g_2 \sin 2\phi)$, where ϕ is the azimuthal angle with respect to the assumed center of the mass distribution. As a measure of the radial surface density profile for the cluster, we use the statistic

$$\zeta^{\rm obs}(r, r_{\rm max}) = \frac{2}{1-(r/r_{\rm max})^2} \int_r^{r_{\rm max}} d\ln(r)\langle g_T \rangle \qquad (4)$$

(Fahlman et al. 1994; Squires et al. 1996a), which gives the mean dimensionless surface density interior to r relative to the mean in the annulus from r to $r_{\rm max}$ in the weak lensing limit:

$$\zeta(r, r_{\rm max}) = \bar{\kappa}(r' < r) - \bar{\kappa}(r < r' < r_{\rm max}) \, .$$

The mean tangential distortion $\langle g_T \rangle$ is calculated by averaging the tangential distortion in an annulus. The value of $\zeta(r)$ provides a lower bound on $\bar{\kappa}(r)$, the mean dimensionless mass surface density within a radius r, and therefore also on the mass within an aperture of radius r. We used a value of 300″ for $r_{\rm max}$. By estimating the mass in the annulus from r to $r_{\rm max}$, one can then estimate the mass within an aperture of radius r.

In Figure 9*a* we show the observed $\langle g_T \rangle$ as a function of radius, using the combined catalog of blue and red background galaxies, which we use as our *best* catalog. In Figure 9*b* the ζ statistic, which provides a lower bound on the mean surface density inside an aperture with radius r, is plotted. It should be noted here that the points and error bars in the $\zeta(r)$ profile are correlated.

A clear lensing signal is detected, although the measurements at small radii are likely to suffer from cluster member contamination. Comparing expected counts to the actual counts indicates that approximately 20% of the galaxies in

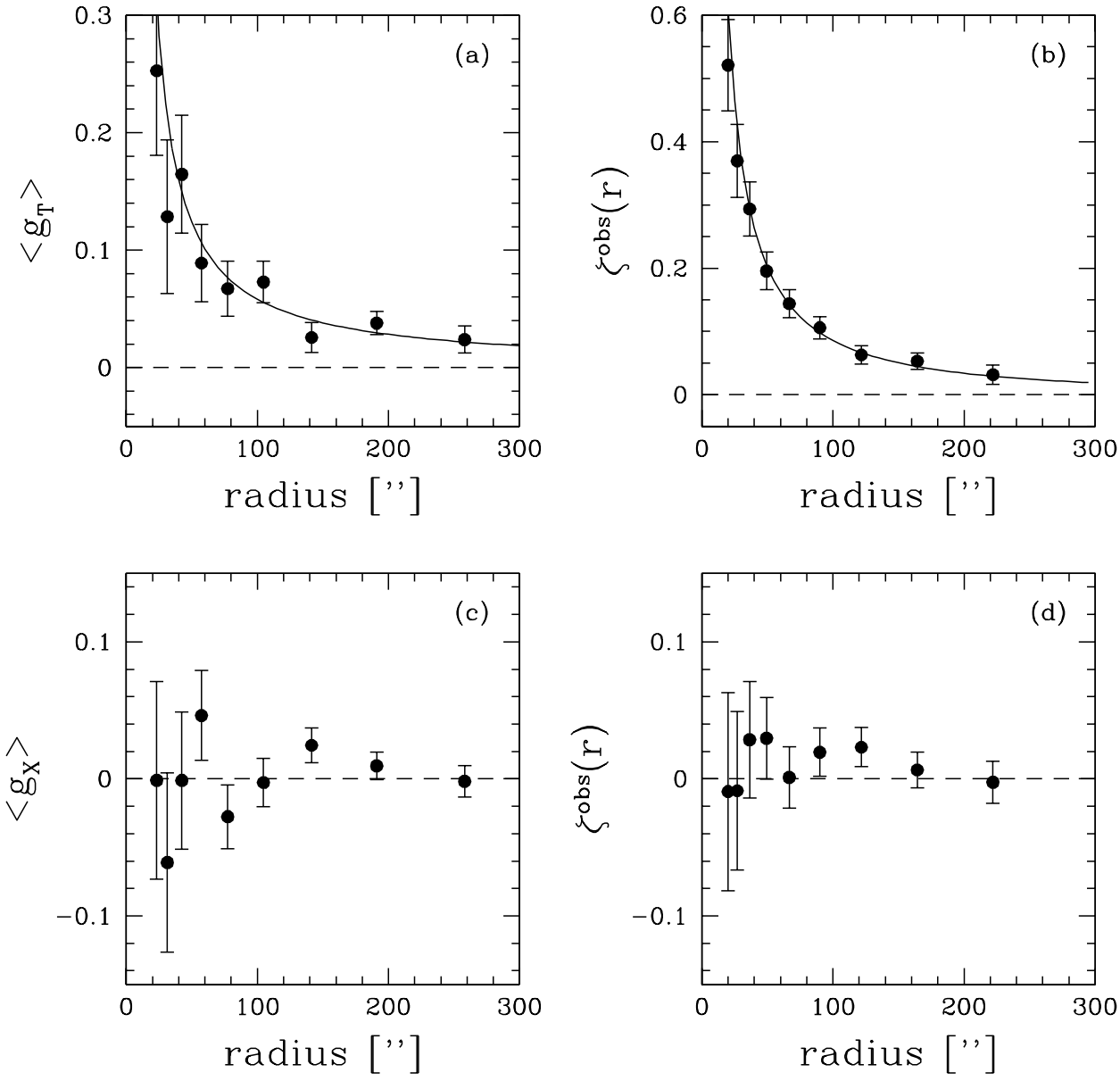

FIG. 9.—(*a*) Mean tangential distortion $\langle g_T \rangle$ as a function of radius from the center as measured from our best sample of background galaxies (combined sample of blue and red galaxies). (*b*) Corresponding ζ profile. The solid lines in (*a*) and (*b*) correspond to the distortion g_T of a singular isothermal sphere with a velocity dispersion of 780 km s^{-1}, which was found by fitting the observations at radii larger than 40″. (*c*) Resulting tangential distortion when the phase of the distortion is increased by $\pi/2$. The signal should vanish if it is due to gravitational lensing. (*d*) The value $\zeta(r)$ corresponding to g_X.

the innermost bin are cluster galaxies. For the faint sample, for which we did not a apply a color correction, we estimate a fraction of 30% cluster members in the innermost bin. Furthermore, we found that the software underestimates the distortion for extremely distorted objects like the bright arc.

We fitted a singular isothermal sphere model to the observations at radii larger than 40″ to minimize the effect of cluster member contamination in the innermost region. The distortion equals the shear divided by $1 - \kappa$. In the calculation of the model distortion, we assume that the background galaxies are located in a sheet behind the cluster at a redshift that corresponds to $\beta = 0.62$.

We find a best fitting value for the line-of-sight velocity dispersion of 780 ± 50 km s^{-1}. The reduced χ^2 of 0.8 indicates that this model fits the data well. The uncertainty quoted reflects only the statistical uncertainty due to the intrinsic ellipticities of the background galaxies. The systematic uncertainty in β, which introduces an additional 10% error at most for the redshift distributions we considered, is not included in the error budget.

As a consistency check we increased the phase of the distortion by $\pi/2$, which is equivalent to rotating all images by 45°. Formally, the surface density corresponding to this distortion is the imaginary part of the surface density. Because the surface density is real, the signal from the rotated distortion should vanish if the observed pattern is due to gravitational lensing. The measured signal, plotted in the lower row in Figure 9, is indeed consistent with being zero.

In Figure 10 we plot the radial profile $\pi r^2 \zeta(r) \Sigma_{\rm crit}$, which is a lower bound on the mass $M(<r)$ within an aperture of radius r, using our best catalog. Calculating a similar profile from the strong lensing model (Franx et al. 1997) yields the dashed line. The open circle in this figure corresponds to the enclosed mass at 21″ given by the strong lensing analysis. The solid line corresponds to the $\zeta(r)$ one would observe for a singular isothermal sphere model with a velocity dispersion of 780 km s^{-1}.

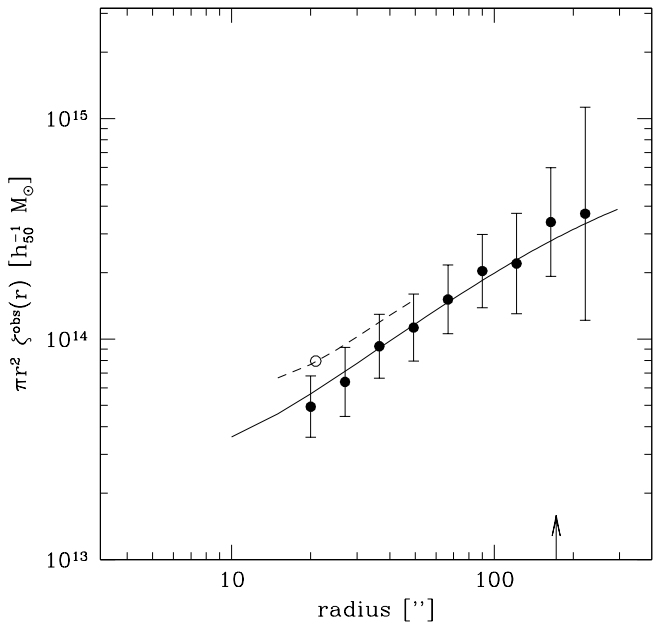

FIG. 10.—Lower bound on the radial mass profile for our best catalog (blue and red galaxies). The error bars only reflect the uncertainty in ζ. The solid line shows the expected profile for our best-fit singular isothermal sphere, which has a velocity dispersion of 780 km s^{-1}. The dashed line corresponds to the profile calculated from the strong lensing model. The open circle gives the enclosed mass at 21″ for a strong lensing model (Franx et al. 1997). The arrow indicates a radius of 1 h_{50}^{-1} Mpc.

From the results of Figure 10 we find from this weak lensing analysis a lower limit on the mass inside an aperture of radius 1 Mpc of $(3.2 \pm 0.9) \times 10^{14}\ M_\odot$. This mass estimate depends only on distortion measurements at radii larger than 1 Mpc. As was expected from the tangential distortion measurements, the profile is well fitted by a singular isothermal model, with a velocity dispersion of 780 km s^{-1} (*solid line*). The projected mass inside 1 Mpc for this model is $(4.4 \pm 0.6) \times 10^{14}\ M_\odot$.

The results from the strong lensing model indicates that the true ζ profile differs from the observed one near the center of the cluster. However, comparing the singular isothermal model to the ζ profile in the outer region of the cluster indicates that this model gives a good estimate for the mass within an aperture of 1 Mpc.

We also calculated the tangential distortion as a function of radius for the various subsamples. The results are shown in the top row of Figure 11. The corresponding $\zeta(r)$ profiles are shown in the bottom row. The solid line indicates the profile of the fit of a singular isothermal model to the tangential distortion at radii larger than 40″. The corresponding velocity dispersions are presented in Table 3. The results for the various subsamples agree well.

The strong lensing mass estimate corresponds to a velocity dispersion of 970 km s^{-1} (Franx et al. 1997), indicating that the weak lensing analysis underestimates the mass near the center of the cluster. Therefore, the surface density profile is steeper than isothermal near the center. This is also supported by the work of Fisher et al. (1998), who find evidence of substructures along the line of sight to the center of the cluster from their kinematical analysis. Such small scale substructures along the line of sight affect the strong lensing analysis more than they do our weak lensing analysis, because we probe the mass distribution on larger scales.

The galaxy used in the strong lensing analysis is at a much larger redshift than the bulk of the galaxies used in the weak lensing analysis. Therefore, a significant cosmological constant can influence our results. Introducing a cosmological constant, however, does not decrease the discrepancy between the weak and strong lensing.

TABLE 3

RESULTS OF FITTING A SINGULAR ISOTHERMAL SPHERE MODEL [$\kappa(r) = \kappa_0/r$] TO THE OBSERVED TANGENTIAL DISTORTION g_T AT RADII LARGER THAN 40″

Name	κ_0 (arcsec)	σ (km s^{-1})
Bright	5.5 ± 1.0	780 ± 70
Faint	4.3 ± 1.0	690 ± 80
Bright + faint	4.9 ± 0.7	740 ± 50
Blue	5.4 ± 0.8	780 ± 60
Red	5.3 ± 1.8	770 ± 130
Blue + red	5.4 ± 0.7	780 ± 50

NOTE.—The second column gives the values found for the model parameter, which corresponds to half the Einstein radius. In the third column the corresponding line-of-sight velocity dispersion is listed, using β listed in the last column of Table 2.

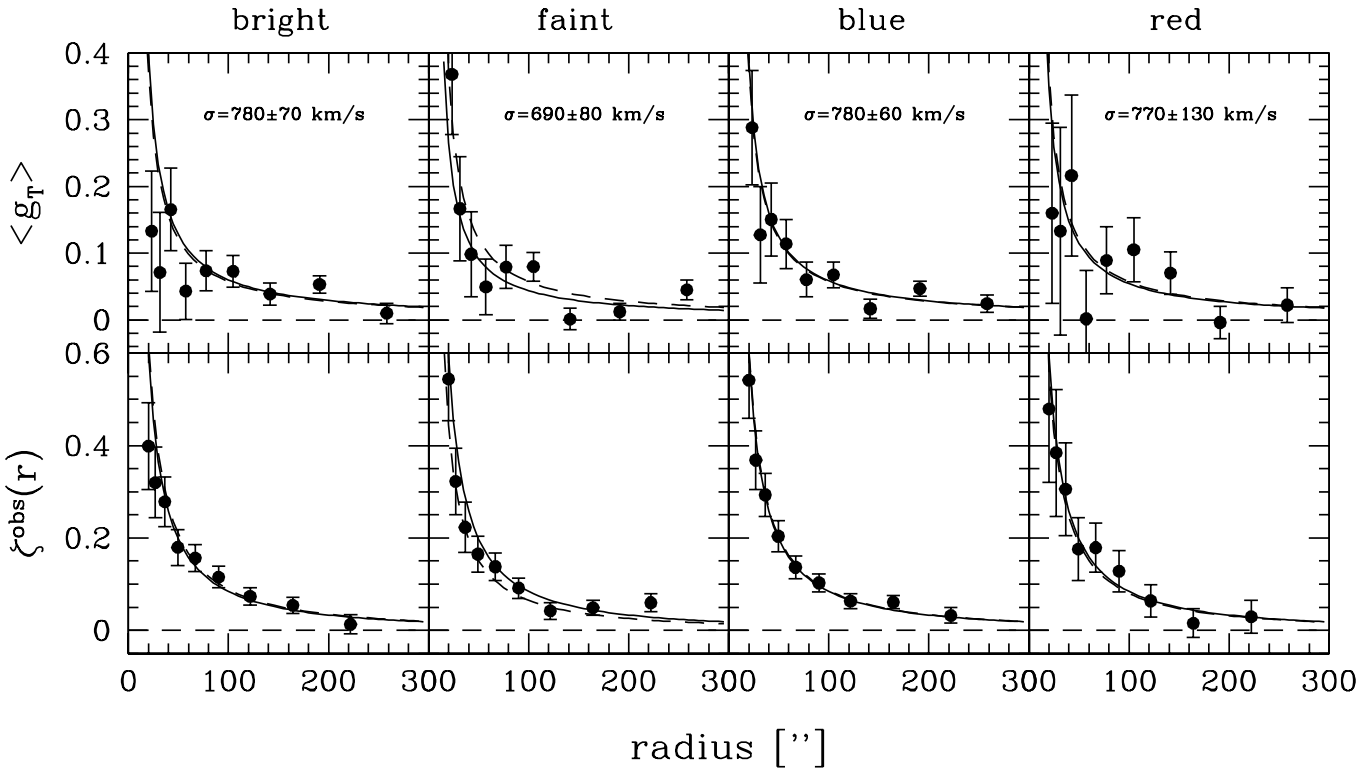

FIG. 11.—Radial tangential distortion profiles for the bright, the faint, the blue, and the red sample (*top panels*); corresponding profiles of the $\zeta(r)$ statistic (*bottom panels*). The solid lines in these figures correspond to the profile of a singular isothermal sphere with a velocity dispersion given in Table 3. The dashed line corresponds to a velocity dispersion of 780 km s^{-1}.

The weak lensing velocity dispersion is lower than those determined through dynamical studies. Fisher et al. (1998) find a velocity dispersion 1027^{+51}_{-45} km s^{-1}. Their velocity dispersion is biased high because of substructures along the line of sight near the center of the cluster. The cluster was also studied by Carlberg et al. (1997), who find 910 $\pm$ 54 km s^{-1}. The weak lensing estimate agrees marginally with this result. We find that the mass distribution is flattened (see § 7.2). Combined with the results of Fisher et al. (1998), this indicates that the cluster might not be dynamically relaxed.

In many clusters from the Canadian Network for Observational Cosmology (CNOC) sample, arcs are observed (e.g., Le Fèvre et al. 1994). For these clusters we estimated the strong lensing velocity dispersion, assuming a singular isothermal model and assuming that the arc is located at the Einstein radius. If the redshift of the arc is unknown, we use $z = 1.5$ and $z = 3$ as a plausible range of source redshifts. Comparing these results to the velocity dispersion measured by Carlberg et al. (1997), we find that both estimates agree fairly well, although the strong lensing estimate tends to be slightly larger than the dynamical value.

Smail et al. (1997) find for their sample of clusters that observed velocity dispersions, estimated from a modest sample of cluster members ($\sim$30), are typically 50% higher than those inferred from their weak lensing analysis. This is quite different from our comparison using strong lensing for CNOC clusters. The agreement with the simple strong lensing models indicates that, in general, the velocity dispersions from Carlberg et al. (1997) are representative of the mass of the cluster. Also, the velocity dispersion inferred from our weak lensing analysis of Cl 1358 is not that far from the observed velocity dispersion.

7.2. *Ellipticity of the Mass Distribution*

As was shown in Schneider & Bartelmann (1996), one can measure the quadrupole moments of the mass distribution directly from the observations, although the expected signal is small. The data we have for Cl 1358 allow us to measure the ellipticity and position angle of the mass distribution directly from the observations.

Although the method described in Schneider & Bartelmann (1996) is model independent, we assume a mass model to relate the strength of the signal to the ellipticity of the mass distribution. A useful deflection potential $\Psi(r, \phi)$ is

$$\Psi(r, \phi) = 2\kappa_0 r[1 - q \cos 2(\phi - \alpha)] , \quad (5)$$

where α is the position angle. The corresponding dimensionless surface density κ is given by

$$\kappa(r, \phi) = \frac{\kappa_0}{r} [1 + 3q \cos 2(\phi - \alpha)] , \quad (6)$$

with an axis ratio $b/a = (1 - 3q)/(1 + 3q)$. For the tangential distortion we can write

$$g_T(r, \phi) = \langle g_T \rangle (1 + g_{2,c} \cos 2\phi + g_{2,s} \sin 2\phi) ,$$

where $g_{2,c} = 3q \cos(2\alpha)$, $g_{2,s} = 3q \sin(2\alpha)$, and $\langle g_T \rangle$ is the mean tangential distortion averaged over a circle. One can measure the axis ratio and position angle by measuring $\langle g_T e^{2i\phi} \rangle$ on a ring. For this model $\langle g_T e^{2i\phi} \rangle = (3/2)q\langle g_T \rangle e^{2i\alpha}$. As an alternative approach, fitting the model tangential distortion to the data yields the axis ratio and position angle. The advantage of this approach is that one does not need data on a complete ring.

In Figure 12 we present the results of the latter procedure. We find that both the flattening and the position angle are constant with radius. For the flattening of the potential, we find $q = 0.18 \pm 0.06$, which corresponds to an axis ratio $b/a = 0.30 \pm 0.15$ for the mass distribution. For the position angle we find $\alpha = -21° \pm 7°$. These results agree well with the elongation of the light distribution in Figure 7 and the mass distribution in Figure 17.

Another model one can use is a singular isothermal ellipsoid (e.g., Kormann, Schneider, & Bartelmann 1994). For this model we can write

$$\frac{\langle g_T e^{2i\phi}\rangle}{\langle g_T\rangle} = \frac{2E[1-(a^2/b^2)] - [1+(a^2/b^2)]K[1-(a^2/b^2)]}{[1-(a^2/b^2)]K[1-(a^2/b^2)]}\, e^{2i\alpha}\,, \tag{7}$$

where $K(k)$ and $E(k)$ are the complete elliptical integral of the first and second kind, respectively. Using equation (7), one can estimate the axis ratio. We measured $\langle g_T e^{2i\phi}\rangle$ out to 170″ from the center. For this model we found a mean position angle of $-18° \pm 10°$ and an axis ratio $b/a = 0.3^{+0.16}_{-0.12}$, similar to what we found previously.

A simple model that reproduces the strong lensing of the $z = 4.92$ galaxy is given by

$$\Psi(x, y) = b\sqrt{r_c^2 + x^2(1-\epsilon) + y^2(1+\epsilon)}\,, \tag{8}$$

which corresponds to an isothermal model with a core radius and axis ratio $[(1-\epsilon)/(1+\epsilon)]^{3/2}$. The best fitting model parameters are $b = 21\farcs05$, $r_c = 12\farcs1$, $\epsilon = 0.3612$, and a position angle of $-17°$. The value for ϵ corresponds to an axis ratio $b/a = 0.32$. Slightly different models give similar results.

The agreement between the weak lensing analysis and the strong lensing results is striking, because the strong lensing

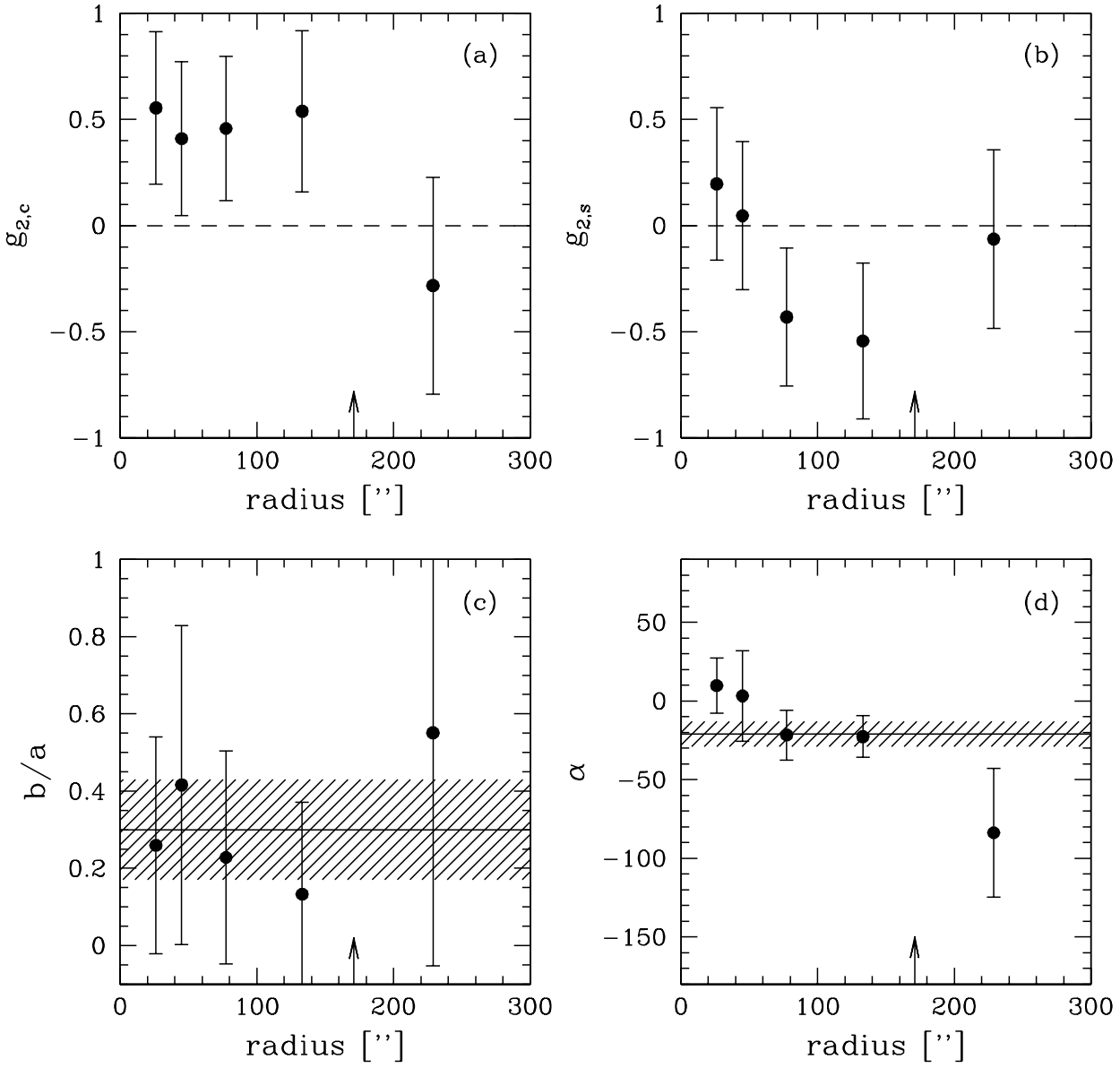

FIG. 12.—(*a*) $g_{2,c} = 3q\cos(2\alpha)$ as a function of radius and (*b*) $g_{2,s} = 3q\sin(2\alpha)$ as a function of radius. (*c*) Measured axis ratio of the mass distribution b/a vs. radius. We find a mean value of $b/a = 0.30 \pm 0.15$ (*shaded region*). (*d*) Position angle α vs. radius. We find a mean $\alpha = -21° \pm 8°$ (*shaded region*). The arrow indicates a radius of 1 h_{50}^{-1} Mpc.

analysis is most sensitive to the mass distribution within the Einstein radius, whereas the weak lensing measurements were done at larger radii.

7.3. *Mass-to-Light Ratio*

To estimate the mass-to-light ratio, we calculated the expected tangential distortion g_L from the observed radial luminosity profile, assuming a constant mass-to-light ratio.

For the light distribution we use the sample of bright cluster galaxies (see § 5). We correct the observed luminosity for the fact that we miss approximately 11% of the light from faint cluster members, using this catalog of cluster galaxies, and calculate the distortion g_L. Comparing the observed distortion to g_L allows us to plot the inferred mass-to-light ratio as a function of radius.

The result, which is shown in Figure 13, is consistent with a constant mass-to-light ratio with a radius out to $\sim 1\ h_{50}^{-1}$ Mpc. Using the procedure described above, we find a value of $90 \pm 13\ h_{50}\ M_\odot\ L_{V\odot}^{-1}$ ($95 \pm 14\ h_{50}\ M_\odot\ L_{V\odot}^{-1}$ for $q_0 = 0.1$). As was the case for the mass estimate, the error in the mass-to-light ratio only reflects the statistical uncertainty due to the random ellipticities of the background galaxies. The uncertainty in the redshift distribution of the background galaxies introduces an extra 10% uncertainty at most for the redshift distributions considered here.

Another estimate for the mass-to-light ratio is obtained using the total mass and light within an aperture of 1 Mpc. Using a total projected mass of $(4.4 \pm 0.6) \times 10^{14}\ M_\odot$, which corresponds to a singular isothermal sphere with a velocity dispersion of 780 km s^{-1} and total luminosity of $(5.19 \pm 0.26) \times 10^{12}\ L_{V\odot}$, we find a mass-to-light ratio of $85 \pm 12\ h_{50}\ M_\odot\ L_{V\odot}^{-1}$. This second estimate depends on the projected mass within 1 Mpc. Using the mass-to-light ratio inferred from the light-traces-mass assumption and the observed luminosity, one finds a mass of $(4.7 \pm 0.6) \times 10^{14}\ M_\odot$ within 1 Mpc, slightly higher than we found by fitting a singular isothermal model to the data.

Studies of the fundamental plane for clusters of galaxies at various redshifts show evidence for galaxy luminosity evolution (van Dokkum & Franx 1996; Kelson et al. 1997). Studying the fundamental plane for Cl 1358, Kelson et al. (1997) find that the mass-to-light ratio in the V band at the redshift of Cl 1358 is $\sim 30\%$ lower than the present-day value. Therefore, the present-day, evolution-corrected mass-to-light ratio would be $117 \pm 17\ h_{50}\ M_\odot\ L_{V\odot}^{-1}$ for Cl 1358.

Cl 1358 is included in the CNOC cluster survey (e.g., Carlberg et al. 1996). Carlberg et al. (1997) find a value of $115 \pm 15\ h_{50}\ M_\odot\ L_{r\odot}^{-1}$ for the mass-to-light ratio of Cl 1358, using a velocity dispersion of 910 ± 54 km s^{-1} and $q_0 = 0.1$. Their luminosity is measured in the Gunn r-band and is K-corrected.

To compare our mass-to-light ratio to the result of Carlberg et al. (1997), we transform our mass-to-light ratio to Gunn r and $q_0 = 0.1$. Using a transformation between $B - r$ and $B - V$ from Jørgensen (1994) and the $B - V$ colors from the results of van Dokkum et al. (1998), we find that our mass-to-light ratio corresponds to a value of $84 \pm 12\ h_{50}\ M_\odot\ L_{r\odot}^{-1}$. This value, which can be compared directly to the value from Carlberg et al. (1997), is lower than the CNOC value. The difference is due to the fact that our weak lensing analysis yields a lower mass than the dynamical analysis.

The range in mass-to-light ratios that Carlberg et al. (1996, 1997) finds is fairly small. Carlberg et al. (1996, 1997) therefore conclude that the mass-to-light ratios of clusters in the CNOC cluster survey are consistent with a universal value. The variance-weighted average mass-to-light ratio for the CNOC sample is $134 \pm 9\ h_{50}\ M_\odot\ L_{r\odot}^{-1}$.

For some of these clusters, ground-based weak lensing analyses are also presented in the literature (Fahlman et al. 1994; Squires et al. 1996b; Smail et al. 1995). Squires et al. (1996b) find a mass-to-light ratio for Abell 2390 that agrees well with the results of Carlberg et al. (1997), whereas Fahlman et al. (1994) find a much higher mass-to-light ratio for MS $1224+20$ from their weak lensing analysis.

Comparing the velocity dispersions found by Carlberg et al. (1997) to simple strong lensing estimates (see § 7.1), we conclude that the observed velocity dispersions are, in general, representative for the cluster mass. Because of substructures along the line of sight, which are an important selection effect for clusters, both the observed velocity dispersions and strong lensing estimates might be slightly biased toward higher masses.

It is therefore difficult to make a firm statement about a universal mass-to-light ratio by comparing our weak lensing results to the result of Carlberg et al. (1997). Furthermore, we only measure the mass-to-light ratio in a fairly small region of the cluster, whereas the CNOC observations extend to larger radii. Furthermore, luminosity evolution in clusters of galaxies (e.g., van Dokkum & Franx 1996; Kelson et al. 1997) needs to be taken into account when comparing clusters at various redshifts. To examine the issue of a universal mass-to-light ratio, more detailed weak lensing measurements of clusters of galaxies are needed.

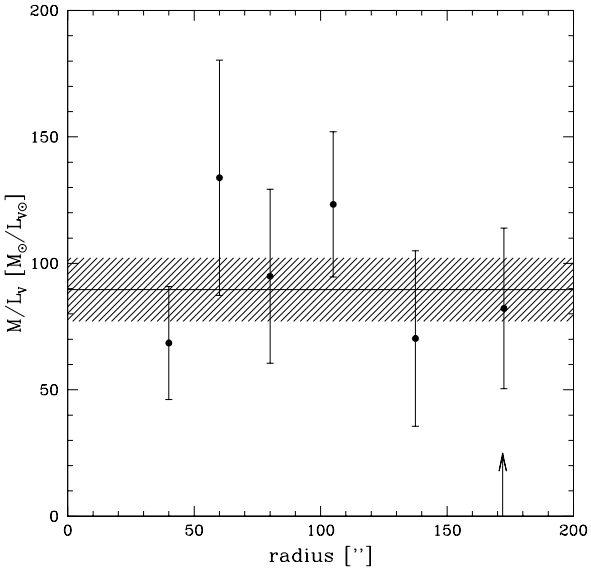

FIG. 13.—Mass-to-light ratio as a function of radius. From a sample of bright cluster galaxies, we estimated the light content over all luminosities using a Schechter luminosity function. The faint end of the luminosity function contributes 11% to the total light. We calculate the tangential distortion g_L corresponding to the light distribution. Under the assumption that the light traces the mass, this allows us to estimate the mass-to-light ratio as a function of radius. The error bars only reflect the uncertainty in the observations. The uncertainty in the redshift distribution of the background galaxies introduces a systematic error of 10% at most. The solid line corresponds to the mean mass-to-light ratio, and the shaded region to the 1 σ uncertainty. The arrow indicates a radius of 1 h_{50}^{-1} Mpc.

7.4. *Two-Dimensional Mass Maps*

In the previous sections we have concentrated on the tangential distortion to estimate the mass and the flattening of the mass distribution of Cl 1358. However, from the observed distortion field one can reconstruct a map of the mass surface density up to an unknown additive constant.

In Figure 14 we present the observed, smoothed distortion field for the best sample of background galaxies (blue and red). We applied a Gaussian smoothing with a scale of 0.4. A clear lensing signal centered on the central galaxy is visible.

In Figure 15 the mass map calculated from our best catalog (blue and red galaxies) is overlaid on the F814W image of Cl 1358. The mass map was calculated using the maximum probability extension of the original KS algorithm (see also Squires & Kaiser 1996). We used 25 wave modes and a regularization parameter $\alpha = 0.05$, and we smoothed the result with a Gaussian of scale 0.4 to allow direct comparison to the maps of the light distribution.

The peak of the mass map corresponds to the peak in the galaxy light distribution. The mass distribution is elongated, roughly in the direction indicated by the results of § 7.2 and shows a tail toward the south. We carried out bootstrap analyses on the actual mass reconstruction maps. It shows that the extension to the south is stable and significant.

Comparison with the number density of galaxies, as was presented in Figure 7, shows that we only reproduce the cluster and not the enhancements in the number density of background galaxies. Because these concentrations were only visible in the faint galaxy counts and were located near the edge of the observed region, one would not expect to recover these concentrations.

Using the original KS algorithm, one can get an estimate of the noise in the mass reconstruction. For a map smoothed with a Gaussian of scale θ, the variance in the dimensionless mass surface density is

$$\langle \kappa^2 \rangle = \frac{\langle \gamma^2 \rangle}{8\pi \bar{n} \theta^2}, \tag{9}$$

where $\langle \gamma^2 \rangle$ is the variance due to the intrinsic shapes of galaxies, for which we found a value of 0.147 from the data. For our catalog we have a number density of 42 galaxies arcmin^{-2}, corresponding to a 1 σ uncertainty of 0.03 in κ. One therefore expects to be able to detect peaks with an associated velocity dispersion of ≥ 500 km s^{-1} at the $\geq 3\ \sigma$ level over the scale of an arcminute (assuming an isothermal model).

We calculated the distortion field corresponding to the mass reconstruction and compared it to the observations. The residual field is shown in Figure 16. The grid shows the layout of the mosaic. At the edges of the mosaic, the residuals increase because of the lower signal-to-noise and, in the center the contribution of cluster members, can cause some residuals.

Similar to what was done in Figure 9, we calculated the mass map after increasing the phase of the distortion by $\pi/2$. The result is shown in the left panel of Figure 17. The reconstruction shows a peak in the lower left corner and a minimum north of the cluster center. According to equation (9) these would correspond to $\sim 3.6\ \sigma$ peaks. Inspection of the catalog shows that the signal is not due to a local peak but is present on scales larger than a WPFC2 chip; therefore, it cannot be an artifact of the camera or the corrections.

Simulations show that the signal-to-noise decreases toward the edges of the region where we have data. Using the dispersion in κ from equation (9), we find that in $\sim 40\%$ of the simulations "$\geq 4\ \sigma$" peaks are present. These peaks occur generally at the edges of the data region. Therefore one cannot trust features in the mass reconstruction that lie near the boundaries. The maximum in the lower left corner of Figure 17*a* is due to the low signal-to-noise in this region. The minimum is located further away from the boundary. We find from our simulations that such minima (or maxima) occur in $\sim 10\%$ of the simulations. Only in the center of the region over which we have data does equation (9) hold.

Although we found a significant elongation of the mass distribution in § 7.2, which is also seen in the mass reconstruction, we find little evidence for substructures in the cluster. Cl 1358 was excluded from the sample of Carlberg et al. (1997) because of its binary nature, but the secondary concentration is outside our data region. The results from Fisher et al. (1998) agree fairly well with the weak lensing mass map. They found two mass concentrations along the line of sight toward the center of the cluster, and a third concentration is found south of the center, corresponding more or less to our extension to the south.

In the literature, much attention has been paid to mass reconstruction methods (KS; Kaiser et al. 1995b; Seitz & Schneider 1995, 1996; Schneider 1995; Squires & Kaiser 1996). Although we use the maximum probability extension of the original KS algorithm, we also calculated a finite-field mass map using the method described in Seitz & Schneider (1996, 1998). The result is shown in Figure 17 (*right panel*). We smoothed the distortion field with the same Gaussian that was used to smooth the mass map from the maximum

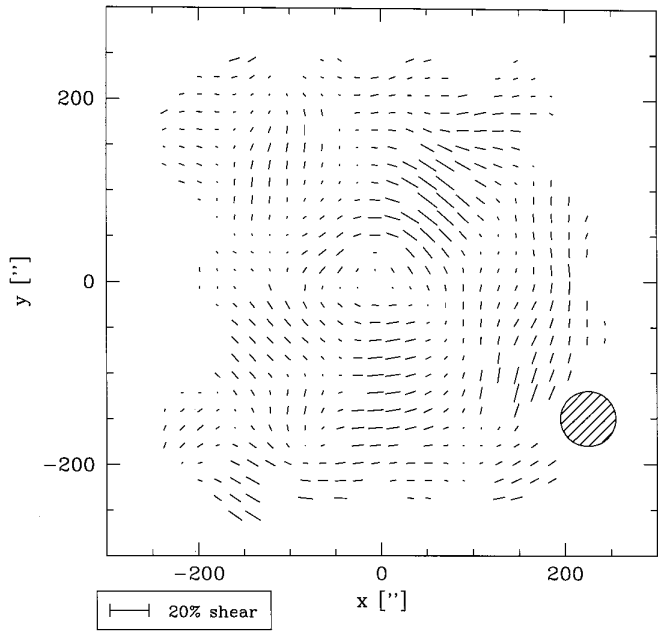

FIG. 14.—Smoothed distortion field g from the blue and red background galaxies. The length of the sticks denote the size of the distortion. The distortion field is calculated by smoothing the observed field from the individual galaxies with a Gaussian of width 0.4 (FWHM is indicated by the shaded circle). The characteristic pattern due to gravitational lensing is clearly visible.

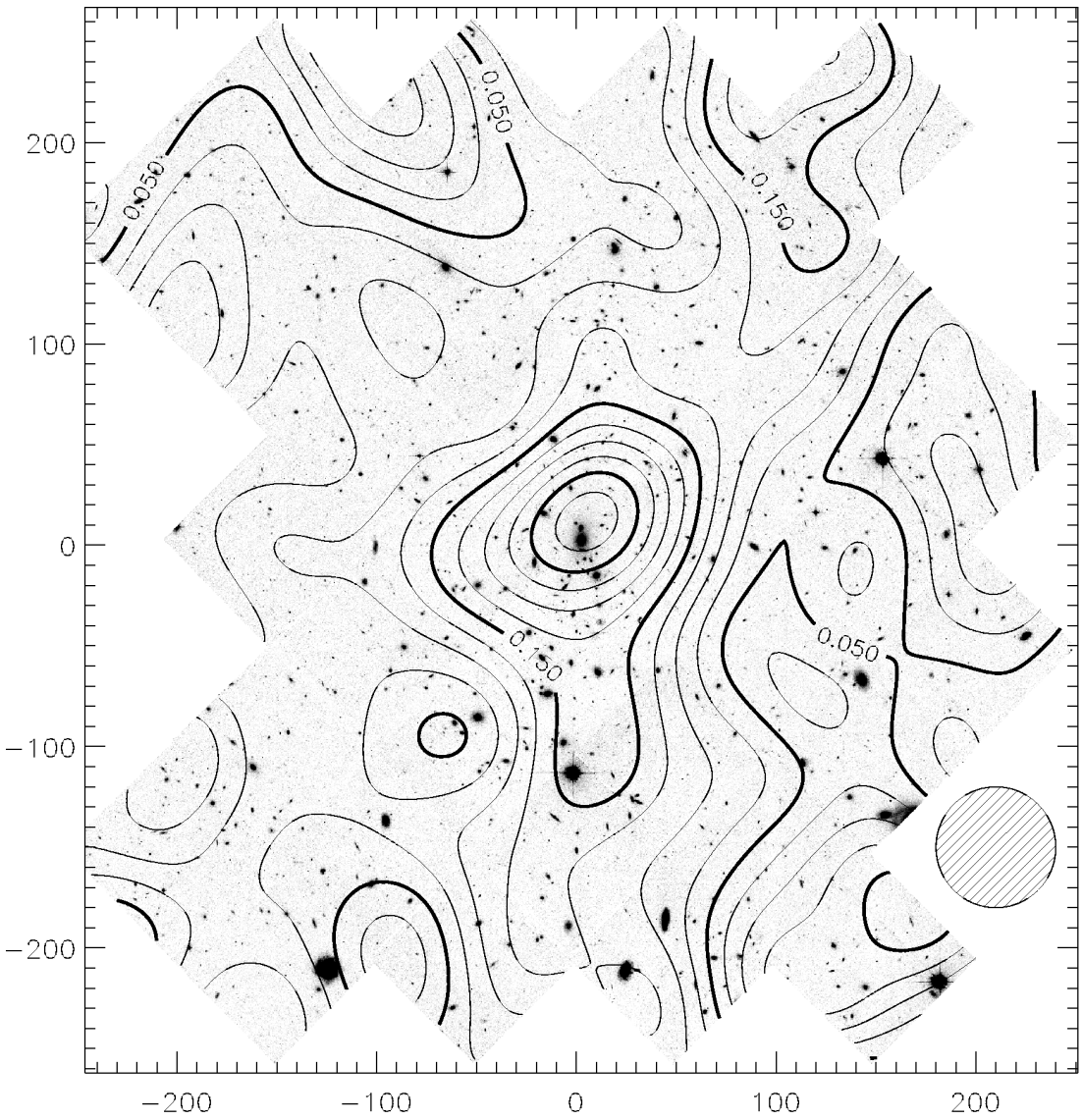

FIG. 15.—Overlay of the reconstructed mass surface density map from our best sample of background galaxies overlayed on the F814W image of Cl 1358. The mass map was calculated using the maximum probability extension of the KS algorithm. The mass map was smoothed with a Gaussian of scale 0.′4 (FWHM, *shaded circle*). The peak in the projected mass distribution coincides with the central elliptical galaxy. The interval between adjacent contour levels is 0.025 in κ. According to eq. (8), 1 σ corresponds to $\sim$0.03 in the central region.

probability method. The two reconstructions are very similar.

7.5. *Comparison to X-Ray Results*

The X-ray emission of Cl 1358 was studied by Bautz et al. (1997), using *ROSAT* and *Advanced Satellite for Cosmology and Astrophysics* (*ASCA*) data. They show that a substantial fraction (10^{44} ergs s^{-1}) of the total X-ray luminosity of $L_X(0.2\text{–}4.5)$ keV $= 7 \times 10^{44}\ h_{50}^{-2}$ ergs s^{-1} is emitted from cool gas, indicating that a cooling flow exists in this cluster. The surface brightness distribution, with PSPC resolution, is unimodal and smooth.

Ignoring the influence of the cooling flow on the integrated *ASCA* spectrum (but accounting for it in the image analysis) and making all the standard assumptions, the *ROSAT* surface brightness profile and the *ASCA* temperature give a preliminary mass of $6.6 \times 10^{14}\ h_{50}^{-1}\ M_\odot$ within 1 Mpc radius (M. Bautz 1997, private communication), although the mass uncertainty is not less than 30%.

Allen (1997) analyzed the *ROSAT* and *ASCA* data on Cl 1358, taking into account the effects of cooling flows on the X-ray images and spectra. The results of Allen (1997) imply a projected mass of $4.2^{+4.1}_{-0.8} \times 10^{14}\ M_\odot$ (90% confidence limits) within an aperture of 1 Mpc from the cluster center, in excellent agreement with the weak lensing mass estimate of $(4.4 \pm 0.6) \times 10^{14}\ M_\odot$, which assumed a singular isothermal sphere model with a velocity dispersion of 780 km s^{-1}.

The gas mass estimated by M. Bautz (1997, private communication) is $6.4 \times 10^{13}\ M_\odot$, with a relative error of at least 15%. Combining the mass of the gas and our weak lensing estimate of the total mass yields a lower limit of $f_b > 0.15\ h_{50}^{-3/2}$ for the baryon fraction, which agrees well with the results of White, Jones, & Forman (1997).

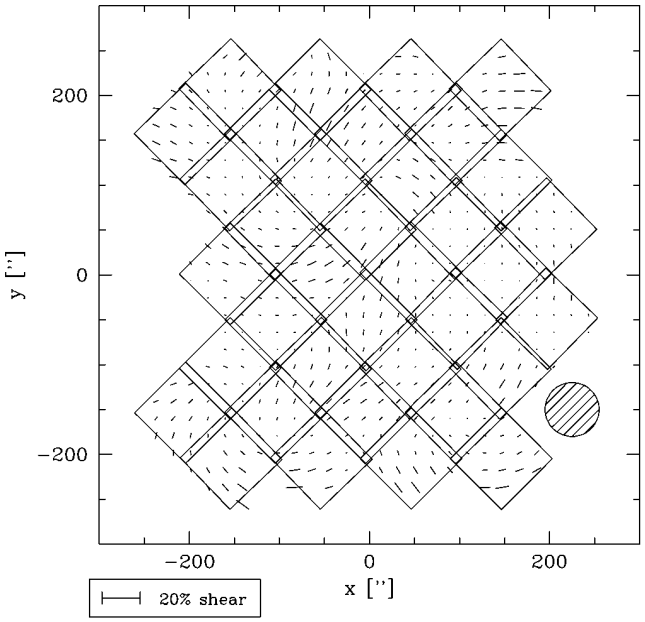

FIG. 16.—Residual field from the smoothed, observed distortion field and the distortion calculated from the mass reconstruction. The length of the sticks denote the size of the distortion. The shaded circle indicates the FWHM of the Gaussian used for the smoothing. The grid shows the layout of the mosaic.

7.6. *Magnification Bias*

Gravitational lensing not only distorts the images of background galaxies, it also magnifies them (e.g., Broadhurst, Taylor, & Peacock 1995; Fort, Mellier, & Dantel-Fort 1996). One consequence of this is that it changes the local number density of background galaxies. Another way of detecting the magnification bias involves measuring the sizes of objects (Bartelmann & Narayan 1995).

The observable number density of background galaxies depends on the relative strength of a deflection effect with respect to a magnification effect. The lens tends to deflect sources away from the center, thus inducing a lower number density, whereas the magnification effect makes the objects larger, thus increasing the detectable number of objects (Broadhurst et al. 1995; Fort et al. 1996; Taylor et al. 1998).

The expected number density of background galaxies is

$$N(r) = N_0\,\mu(r)^{2.5\alpha-1}\,,$$

where μ is the magnification at radius r, and α is the slope of the galaxy counts $d\log(N)/dm$.

It is found that the count slopes for red objects are lower than those found for blue objects (Broadhurst et al. 1995). Such an effect would result in a decrease of the ratio of the number density of red over blue objects toward the center of the cluster. We used our catalog of objects detected in both F606W and F814W. The red sample is created using all objects having F606W − F814W > 1.4 and 24 < F814W < 26.5. The blue sample is defined by objects with F606W − F814W < 0.8 and 24 < F814W < 26.5. This large separation in color gives a minimal contribution from cluster galaxies. The count slopes $\alpha_{\rm red} \approx 0.25$ and $\alpha_{\rm blue} \approx 0.45$ indicate that one could measure the magnification, given a signal that is strong enough.

In Figure 18 we plot the ratio of number densities of red and blue objects as a function of radius. The solid line shown in this figure shows the expected signal for a singular isothermal sphere with a velocity dispersion of 780 km s^{-1}. This already shows that the expected signal is small. Given the fairly low expected signal-to-noise for this method, our measurements are consistent with a constant ratio, i.e., consistent with no detectable magnification.

This method to detect a magnification bias, however, suffers from several problems. The results are very sensitive to clustering of the background objects. A local lack of red objects could either be due to the bias or only to a real underdensity of red objects. Furthermore, the Poisson noise on the counts is fairly large compared to the expected signal.

An argument for measuring the magnification bias from

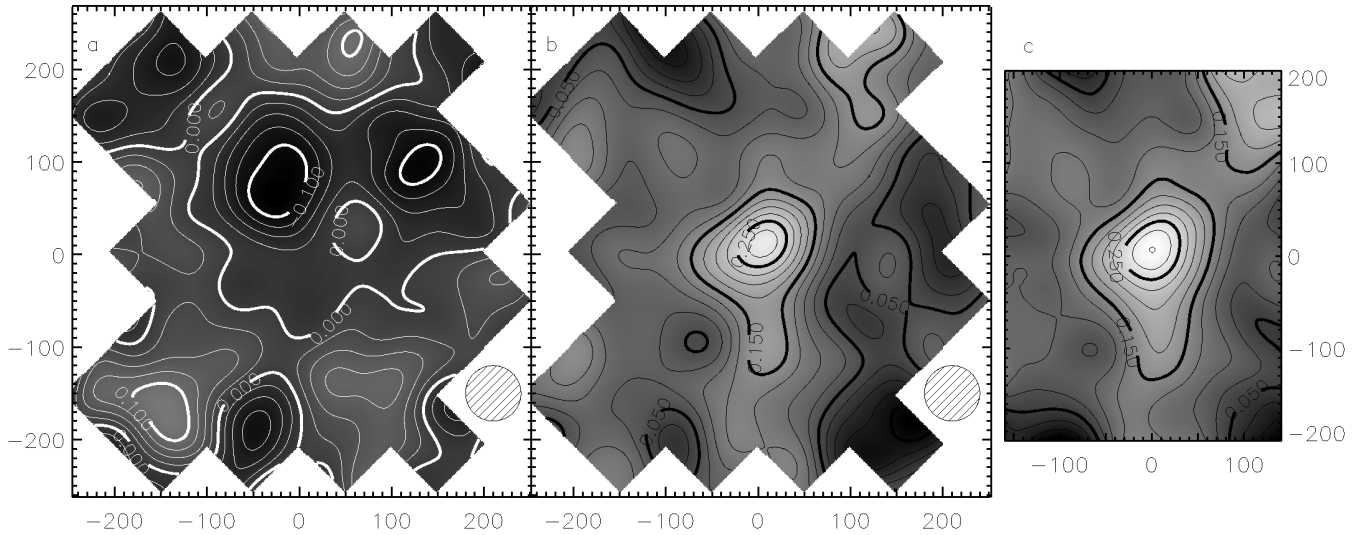

FIG. 17.—(*a*) Mass surface density reconstruction when the phase of the distortion is increased by $\pi/2$. This should vanish if the signal is due to gravitational lensing. (*b*) Mass reconstruction of the best catalog (see Fig. 15). (*c*) Result from a finite field mass reconstruction algorithm developed by Seitz & Schneider (1996, 1998). The interval between adjacent contours is 0.025 in κ. According to eq. (8), 1 σ corresponds to 0.03 near the center. All three mass reconstructions were smoothed with a Gaussian of scale 0.′4. The shaded circles show the FWHM of this smoothing function.

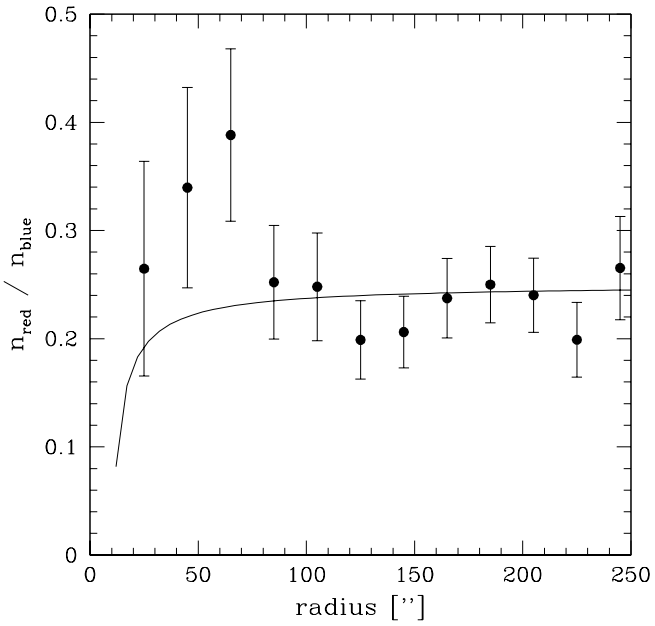

FIG. 18.—Ratio of the number density of red objects and blue objects as a function of radius from the cluster center. The plotted points are independent measurements of this ratio. Red objects have a F606W − F814W color ≥ 1.4 and blue objects have F606W − F814W ≤ 0.8. The solid line indicates the expected signal for a singular isothermal sphere with a velocity dispersion of 780 km s^{-1}. The measurements are consistent with a constant ratio.

number counts is that one does not require extremely good seeing, because one only counts objects. The data presented in the paper here yield high number densities of background galaxies. Comparing the null detection of the magnification bias to the results of the shear measurements shows that measuring the magnification bias through number counts is hard for most clusters of galaxies. For very massive clusters, however, the magnification signal might be detected (Taylor et al. 1998).

8. CONCLUSIONS

We have mapped the light and mass distributions of the cluster of galaxies Cl 1358+62, using a large mosaic of *HST* observations in F606W and F814W. The total field of view of these observations is approximately $8' \times 8'$. This provides us with an ideal data set for a weak lensing analysis of the cluster.

The WFPC2 PSF is highly anisotropic at the edges of the individual chips. This systematically distorts the shapes of the faint background galaxies. We improved the correction technique developed by KSB95 and LK97 and used it to correct the shapes for PSF effects. We exclude galaxies with a scale length less than 1.2 pixels, because simulations show that these object cannot be corrected well. We show that this scheme allows a straightforward correction for shear introduced by camera distortion.

We detect 4175 objects with scale lengths larger than 1.2 pixels, corresponding to a number density of 79 galaxies arcmin^{-2}. From this catalog we select a sample of blue and red background galaxies, which contains 2228 galaxies (42 galaxies arcmin^{-2}).

We detect a weak lensing signal out to ~ 1.5 Mpc from the cluster center. Fitting a singular isothermal sphere model to the observed tangential distortion shows that the data are consistent with a singular isothermal sphere with a velocity dispersion of 780 ± 50 km s^{-1}. For this model, the corresponding projected mass within a radius of 1 Mpc from the cluster center is $(4.4 \pm 0.6) \times 10^{14}\ M_\odot$. The errors quoted here only include the statistical uncertainty due to the intrinsic ellipticities of the background galaxies. The uncertain redshift distribution of these background sources introduces an additional systematic error of at most 10% for the redshift distributions considered here.

The weak lensing velocity dispersion is lower than the dynamical estimates of 1027^{+51}_{-45} km s^{-1} (Fisher et al. 1998) and 910 ± 54 km s^{-1} (Carlberg et al. 1996). A strong lensing model with a velocity dispersion of 970 km s^{-1} (Franx et al. 1997) indicates that the weak lensing analysis underestimates the mass in the central region and that the projected mass profile is steeper than isothermal in the center.

Comparing the observed velocity dispersions of cluster in the CNOC sample (Carlberg et al. 1997) to simple strong lensing estimates, we find no evidence that the observed velocity dispersions are much higher than those inferred from lensing (Smail et al. 1997). Therefore, the velocity dispersions measured by Carlberg et al. (1997) are in general representative for the cluster masses.

A kinematical study of Cl 1358 by Fisher et al. (1998) shows that there are two mass concentrations along the line of sight, of which one corresponds to the brightest cluster galaxy and its companions. This elongation, as well as the flattening of the projected mass distribution, can increase the observed velocity dispersion.

The projected mass within 1 Mpc inferred from X-ray observations is $(4.2^{+4.1}_{-0.8}) \times 10^{14}\ M_\odot$ (90% confidence; Allen 1997), in good agreement with the weak lensing mass. (M. Bautz 1997, private communication) estimated the total gas mass to be $(6.4 \pm 1.0) \times 10^{13}\ M_\odot$. Combining this result with the weak lensing mass yields a lower limit of $f_b > 0.15\ h_{50}^{-3/2}$ for the baryon fraction, in good agreement with White et al. (1997).

The elongation of the mass distribution is measured directly from the data. We find that the mass distribution is elongated with a position angle of $-21° \pm 7°$ measured from the north. Assuming an ellipsoidal mass distribution, we find an axis ratio of 0.3 ± 0.15. This result agrees well with what is found from the light distribution and the mass reconstruction.

A strong lensing analysis based on the red arc (Franx et al. 1997) gives nearly the same results: a position angle of $-17°$ and an axis ratio $b/a = 0.32$. As the weak and strong lensing analyses are probing different regions in the cluster, the results indicate that the flattening and position angle of the mass distribution are fairly constant with radius.

To map the total projected mass distribution, we used the maximum probability extension of the original KS algorithm (KS; Squires & Kaiser 1996). We compared the resulting mass map to the result from a finite field reconstruction algorithm developed by Seitz & Schneider (1996, 1998). The two mass maps are very similar.

The peak of the reconstructed mass distribution coincides with the central elliptical galaxy and the peak of the light distribution. Also, the overall shape resembles that of the light. The reconstruction shows an extension to the south, as is seen in the optical light.

Assuming a constant mass-to-light ratio, we calculated

the tangential distortion corresponding to the observed radial light profile. Comparing the result to the observed distortion yields the mass-to-light ratio, provided that the light traces the mass. We find that the mass-to-light ratio is consistent with being constant with radius and estimate a value of $(90 \pm 13) h_{50} M_{\odot} L_{V\odot}^{-1}$.

The corresponding mass-to-light ratio in Gunn r (and $q_0 = 0.1$) is $(84 \pm 12)\ h_{50}\ M_{\odot}\ L_{r\odot}^{-1}$ and is lower than the value of $(115 \pm 15) h_{50} M_{\odot} L_{r\odot}^{-1}$ measured by Carlberg et al. (1997), because of the fact that we derive a lower mass for Cl 1358.

Our mass-to-light ratio is significantly lower than the average mass-to-light ratio found from the sample of clusters in the CNOC cluster survey (Carlberg et al. 1996; Carlberg et al. 1997). From the results presented in this paper, it is, however, not possible to make a firm statement about the universality of cluster mass-to-light ratios. Because of substructures along the line of sight, the CNOC results might be biased somewhat high. Furthermore, we only probe a fairly small region of the cluster compared to Carlberg et al. (1997). Comparing clusters at various redshifts, luminosity evolution needs to be taken into account (e.g., van Dokkum & Franx 1996; Kelson et al. 1997). To investigate the issue of a universal mass-to-light ratio in more detail, more detailed weak lensing analyses of clusters of galaxies are needed.

The analysis presented in this paper shows that mosaics of *HST* observations provide an excellent opportunity to do detailed weak lensing studies of clusters of galaxies. The high number density of background objects, combined with the small corrections for the size of the PSF allow us to calculate high-resolution mass maps and precise mass estimates.

The authors would like to thank Nick Kaiser for making the IMCAT software available. It is a pleasure to thank Peter Schneider for useful discussions and for making available his mass reconstruction method. We also thank Caryl Gronwall, Rychard Bouwens, Joseph Silk, and Harry Ferguson for providing their $n(m, z)$ distributions, and Mark Bautz for sharing his information on the X-ray observations. The initial data reduction, done by Pieter van Dokkum, is obviously invaluable for this analysis. The comments from the referee, Gary Bernstein, helped to clarify the paper significantly.

APPENDIX A

CORRECTING FOR THE PSF AND CAMERA DISTORTION

The PSF and the camera distortions change the shapes of the galaxies needed for the weak lensing analysis. The effect of the PSF is a smearing and depends on the size of the object. A camera distortion introduces a genuine shear, which is independent of the size of the object but depends on its shape. One must correct the shapes of the galaxies for these effects.

A1. CORRECTING FOR THE PSF

To estimate the shear from our observations, we followed the method described in KSB95 and LK97. The *HST* observations differ from usual ground-based observations in the sense that the *HST* PSF is badly sampled and that the PSF is anisotropic at large radii. It is therefore not obvious that the correction scheme described in KSB95 can be applied to *HST* data. We examined the derivation presented in KSB95 and tested the method by simulations.

To quantify the distortion, we combine the quadrupole moments to form a two-component polarization:

$$e_1 = \frac{I_{11} - I_{22}}{I_{11} + I_{22}} \qquad \text{and} \quad e_2 = \frac{2I_{12}}{I_{11} + I_{22}} \tag{10}$$

(Blandford et al. 1991).

To suppress divergent sky noise contributions in the measurements of the quadrupole moments, we use a Gaussian weight function. Thus the quadrupole moments are evaluated using

$$I_{ij} = \int d^2\theta W(\theta)\theta_i \theta_j f(\theta)\ . \tag{11}$$

Here $(\theta_1, \theta_2) = (0, 0)$ is the assumed center of the object. The center is chosen to be the point where the weighted dipole moments are zero. We use a Gaussian with a dispersion that is proportional to r_g, the radius of maximum significance (this radius is given by the peak finder; KSB95). For such a weighting scheme, the first-order shift in polarization due to the shear is given by

$$\delta e_{\alpha} = P_{\alpha\beta}^{\rm sh} \gamma_{\beta}\ , \tag{12}$$

where the shear polarizability $P_{\alpha\beta}^{\rm sh}$ is given by

$$P_{\alpha\beta}^{\rm sh} = X_{\alpha\beta}^{\rm sh} - e_{\alpha} e_{\beta}^{\rm sh}\ , \tag{13}$$

and where $X^{\rm sh}_{\alpha\beta}$ and $e^{\rm sh}_{\alpha}$ are defined as

$$X^{\rm sh}_{\alpha\beta} = \frac{1}{I_{11}+I_{22}} \int d^2\theta \begin{bmatrix} 2W\theta^2 + 2W'(\theta_1^2-\theta_2^2)^2 & 4W'(\theta_1^2-\theta_2^2)\theta_1\theta_2 \\ 4W'(\theta_1^2-\theta_2^2)\theta_1\theta_2 & 2W\theta^2 + 8W'\theta_1^2\theta_2^2 \end{bmatrix} f(\boldsymbol{\theta}) \tag{14}$$

and

$$e^{\rm sh}_{\alpha} = 2e_{\alpha} + \frac{2}{I_{11}+I_{22}} \int d^2\theta \begin{pmatrix} \theta_1^2-\theta_2^2 \\ 2\theta_1\theta_2 \end{pmatrix} W'\theta^2 f(\boldsymbol{\theta}) \,, \tag{15}$$

where W' denotes the derivative of W with respect to θ^2. The shear polarizability gives the response of an object to an applied shear and can be calculated from the data. Note, however, that equation (15) differs from B12 in KSB95. This difference is significant for elongated objects. Also, the effect of seeing is not included in this estimate of the shear polarizability. LK97 present a nice way to solve this problem.

An anisotropic PSF changes the shapes of observed objects. Before applying equation (12), one must therefore correct the measured polarizations for this effect. KSB95 give a correction if the PSF anisotropy can be written as a convolution of a small, normalized, anisotropic PSF with a circular seeing disc. Such a PSF changes the quadrupole moments according to

$$I'_{ij} = I_{ij} + q_{lm} Z_{lmij} \,, \tag{16}$$

where q_{lm} are the unweighted quadrupole moments of the PSF and where Z_{lmij} is given by

$$Z_{lmij} = \frac{1}{2} \int d^2\theta f(\boldsymbol{\theta}) \frac{\partial^2 [W(\boldsymbol{\theta})\theta_i\theta_j]}{\partial\theta_l \partial\theta_m} \,. \tag{17}$$

This equation is similar to equation (A4) in KSB95 except for the factor $\frac{1}{2}$. The change in polarization due to an anisotropy in the PSF is given by

$$\delta e_{\alpha} = P^{\rm sm}_{\alpha\beta} p_{\beta} \,, \tag{18}$$

where $p_{\alpha} \equiv (q_{11}-q_{22}, 2q_{12})$ is a measure of the PSF anisotropy, and where $P^{\rm sm}_{\alpha\beta}$ is the smear polarizability, defined as

$$P^{\rm sm}_{\alpha\beta} = X^{\rm sm}_{\alpha\beta} - e_{\alpha} e^{\rm sm}_{\beta} \,, \tag{19}$$

and where $X^{\rm sm}_{\alpha\beta}$ and $e^{\rm sm}_{\alpha}$ are given by

$$X^{\rm sm}_{\alpha\beta} = \frac{1}{I_{11}+I_{22}} \int d^2\theta \begin{bmatrix} W + 2W'\theta^2 + W''(\theta_1^2-\theta_2^2)^2 & 2W''(\theta_1^2-\theta_2^2)\theta_1\theta_2 \\ 2W''(\theta_1^2-\theta_2^2)\theta_1\theta_2 & W + 2W'\theta^2 + 4W''\theta_1^2\theta_2^2 \end{bmatrix} f(\boldsymbol{\theta}) \tag{20}$$

and

$$e^{\rm sm}_{\alpha} = \frac{1}{I_{11}+I_{22}} \int d^2\theta \begin{pmatrix} \theta_1^2-\theta_2^2 \\ 2\theta_1\theta_2 \end{pmatrix} (2W' + W''\theta^2) f(\boldsymbol{\theta}) \,, \tag{21}$$

where the prime denotes differentiation with respect to θ^2.

Apart from a factor of $\frac{1}{2}$, equation (21) is slightly different from equation (A12) in KSB95. The effect of this difference is fairly small and was therefore not noticed in previous simulations. These differences were also noticed independently by H. Hämmerle 1997 (private communication).

According to equation (16), one should use the unweighted quadrupole moments of the stars to quantify the anisotropy of the PSF. We use a different estimate

$$p_{\alpha} = \frac{e^*_{\alpha}}{P^{\rm sm*}_{\alpha\alpha}} (r_g) \,, \tag{22}$$

where the asterisk indicates that the parameters are calculated from the stars. We use the same weight function that was used to calculate the parameters of the object we want to correct. In KSB95 a similar estimate for p_{α} is used, although there the weight function used to calculate the PSF parameters is not matched to the object one wants to correct.

As is demonstrated below, the original KSB95 scheme cannot be applied to more complex PSFs. As mentioned above the correction holds if the PSF can be described as a convolution of a postseeing circularly smeared image with a small anisotropic PSF. The *HST* PSF cannot be described this way. Oversampled PSFs calculated by Tiny Tim[3] (Krist & Hook 1996) show that the anisotropy is mainly caused by the anisotropy of the diffraction rings.

As a compromise, we adapt the weight function when calculating PSF parameters. In Appendices B, C, and D, our choice is justified. Although it is not a perfect scheme, the simulations presented in the Appendices below show that our approach works fairly well.

Having corrected for the PSF anisotropy, one still needs to calculate the shear from the measured polarizations. The calculated shear polarizability gives a good estimate in the absence of seeing. The polarizations of small objects, however, are

[3] Available at http://www.stsci.edu/ftp/software/tinytim.

decreased because the PSF circularizes objects. Up to now people used *HST* images to estimate the correction factor for their ground-based observations (KSB95). A similar scheme is not at hand when using *HST* data.

Fortunately, LK97 present a very useful way to calculate a "preseeing" shear polarizability:

$$P^{\gamma} = P^{\rm sh} - \frac{P^{\rm sh}_*}{P^{\rm sm}_*} P^{\rm sm} , \tag{23}$$

where the asterisk denotes once more values measured from the stars. This "preseeing" shear polarizability can be calculated directly from the observations.

In LK97 nothing is mentioned about the weighting one should use. The weight function that is used in the analysis of the galaxies is a Gaussian with a scale length r_g, equal to the value given by the peak finder. But in principle one might take any weight function.

This issue is important because, in general, $P^{\rm sh}_*/P^{\rm sm}_*$ will be different for different r_g. An intuitive guess is that $P^{\rm sh}_*$ and $P^{\rm sm}_*$ have to be calculated from the star using the same weight function as was used in calculating the polarizabilities for the object one wants to correct, similar to what we found for the correction for the PSF anisotropy. In Appendices C and D this is investigated in more detail.

A2. CORRECTING THE CAMERA DISTORTION

The shear introduced by camera distortion is usually small. However, using the results of the previous section, one can easily correct for this effect. The derivation is similar to that leading to the "preseeing" shear polarizability in LK97.

We measure the polarization and polarizabilities of stars and galaxies from our observations. In the previous section we did not take the effect of a camera shear into account. Such a shear δ changes the shape of a star:

$$e^{\rm obs}_* = e_* + P^{\rm sh}_* \delta , \tag{24}$$

where e_* is the polarization of the star in the absence of a camera distortion and $e^{\rm obs}_*$ the observed polarization. For a galaxy we measure a polarization

$$e^{\rm obs} = e^{\rm true} + P^{\gamma}\gamma + \frac{P^{\rm sm}}{P^{\rm sm}_*} e^{\rm obs}_* + P^{\rm sh}\delta , \tag{25}$$

with $e^{\rm true}$ the intrinsic polarization of the galaxy and γ the shear due to gravitational lensing. Using equation (24) we get

$$e^{\rm obs} = e^{\rm true} + P^{\gamma}\gamma + P^{\rm sm}\frac{e_*}{P^{\rm sm}_*} - P^{\rm sh}\frac{P^{\rm sh}_*}{P^{\rm sm}_*}\delta + P^{\rm sh}\delta . \tag{26}$$

To correct for the PSF anisotropy, we use the observed polarization of the stars in equation (2). Thus we find that

$$e^{\rm obs} = e^{\rm true} + P^{\rm sm}p + P^{\gamma}(\gamma + \delta) , \tag{27}$$

where p is $e^{\rm obs}_*/P^{\rm sm}_*$.

After correcting for the PSF anisotropy, one finds that the observed shear is equal to $\gamma + \delta$. To correct for the camera distortion, one just has to subtract δ from the observed shear field.

APPENDIX B

ANISOTROPY CORRECTION

In KSB95 the authors quantify the anisotropy of the PSF, p_α, by dividing the polarization of a star by its smear polarizability. They implicitly assume that the value of p_α thus derived does not depend on the weight function; formally, it corresponds to the unweighted quadrupole moments of the PSF.

The *HST* PSF is fairly complicated, and therefore we tested several correction schemes for the PSF anisotropy: (1) p_α calculated with a weight function of size matched to the stellar image, as in KSB95, (2) using the true p_α (unweighted), and (3) using a weight function of size matched to the galaxy image to be corrected.

In the simulations we used objects with exponential profiles of different sizes. These objects were convolved with 10 times oversampled model PSFs, calculated by Tiny Tim (Krist & Hook 1996), block averaged to WPFC2 resolution, and convolved with the pixel scattering function as given in the Tiny Tim manual. In order to address the effect of undersampling, objects were placed at different positions with respect to the pixel grid.

The results are shown in Figure 19. The error bars indicate the scatter in the polarization measurements due to undersampling effects: clearly e_1 is more sensitive to this problem than e_2. Figures 19*b*–19*d* and 19*f*–19*h* show the results of the different PSF anisotropy correction schemes. The results in Figures 19*d* and 19*h* are obtained using the scheme we advocate and use in this paper, and they show that this approach performs best. The simulations show that the undersampling does not cause a bias in the estimation of the corrected polarization.

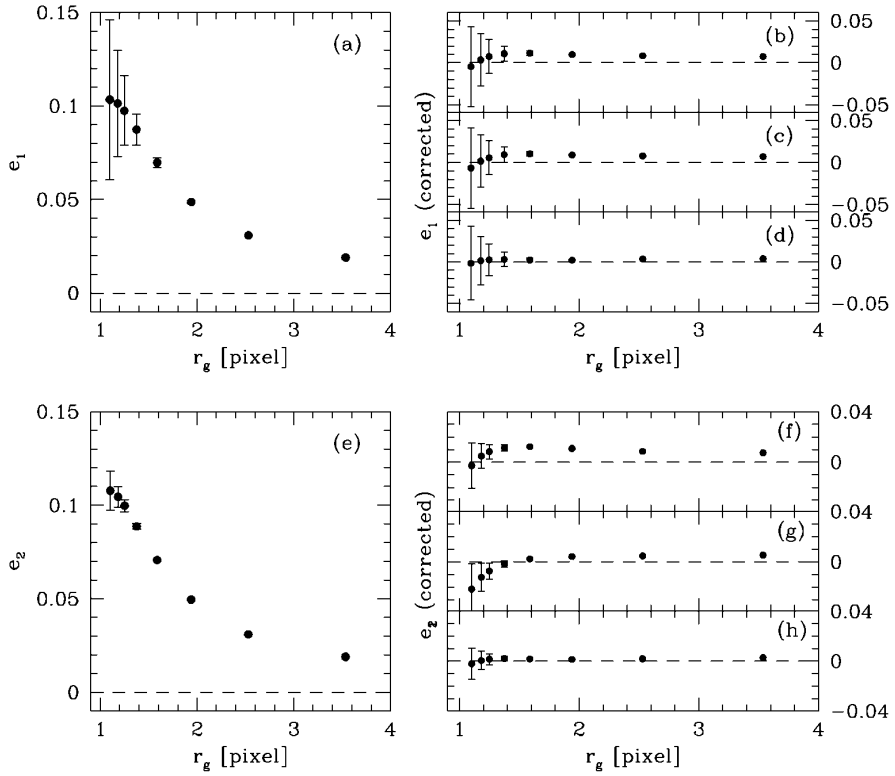

FIG. 19.—Simulations of the correction for PSF anisotropy. (*a*) Measured e_1 for objects with exponential profiles that have an intrinsic e_1 of zero as a function of the size of the object. The error bars shown indicate the scatter in the measurement of the polarization due to sampling. (*e*) Results for a similar simulation, but now for e_2. (*b*, *c*, *d*, *f*, *g*, and *h*) Corrected polarizations for the various correction schemes. The results shown in (*b*) and (*f*) were obtained using p_α as indicated in KSB95. (*c*, *g*) Results using unweighted moments for the stars; (*d*, *h*) results when the weight function for the stars is identical to that of the corrected object.

APPENDIX C

"SEEING" CORRECTION

Here we first investigate the correction for PSF–induced circularization presented in LK97. We first consider an almost "round" PSF, calculated by Tiny Tim (Krist & Hook 1996). Although we apply a small anisotropy correction, this way we

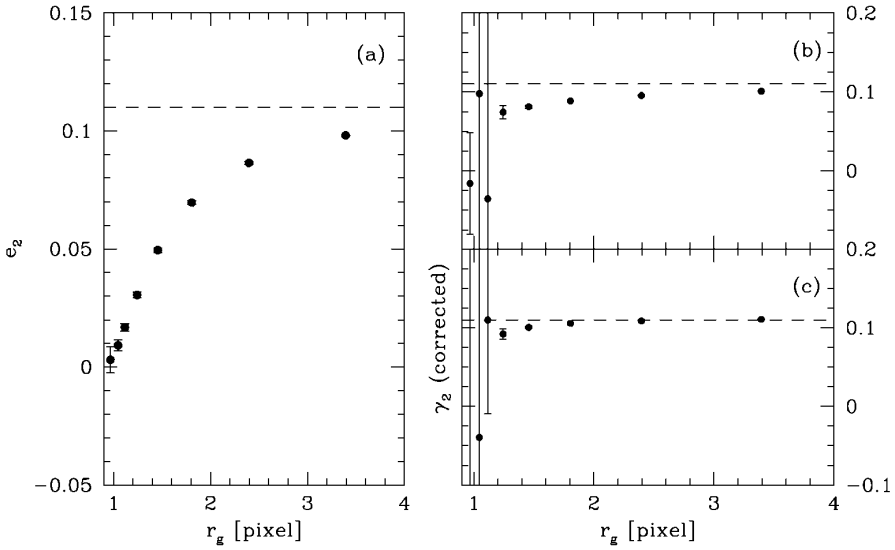

FIG. 20.—Simulation of the correction for "seeing," using an almost circular PSF. (*a*) Measured e_2 for objects with exponential profiles to which we applied a shear γ_2 of 11% (*dashed line*). The error bars shown indicate the scatter in the measurement of the polarization due to sampling. (*b*) Measured shear using the LK97 formalism. The polarizabilities of the stars were calculated using a Gaussian weight function with a scale length equal to the scale length of the stars. (*c*) Results using a Gaussian weight function with a scale length equal to the scale length of the corrected object.

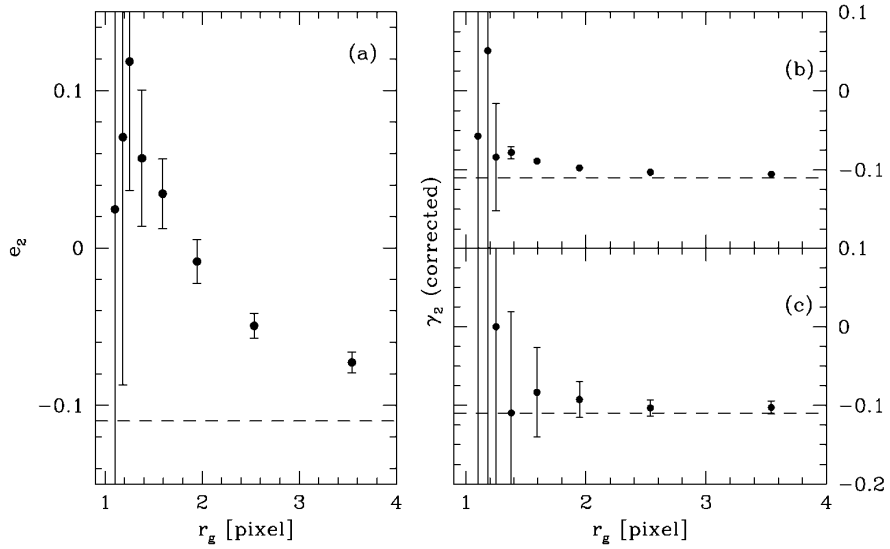

FIG. 21.—Simulation of the correction for the PSF effects. (*a*) Measured e_2 for objects with exponential profiles, to which we applied a shear γ_2 of -11% (*dashed line*). In this simulation, we added noise. The error bars shown indicate the scatter in the measurement of the polarization due to sampling and noise. (*b*) Measured shear in the same simulation, in the absence of noise. (*c*) Results in the simulation with noise. In both cases the results are similar, although the error is very large for small objects when noise is present.

can examine the LK97 formalism accurately. The anisotropy correction we used is the one advocated in this paper.

In Figure 20 we show the results of such a simulation, in which objects of different sizes are sheared, convolved with the Tiny Tim PSF, and analyzed with the LK97 formula. We applied a shear $\gamma_2 = 0.11$. Figure 20*a* shows the measured polarizations as function of the size of the object. Figure 20*b* shows the recovered shear using parameters for the stars, calculated with a constant weight function. Even for large objects, the recovered shear is lower than the applied value. The results shown in Figure 20*c* show that the correction scheme we adopt in this paper performs best, although the recovered shear is slightly underestimated for small objects. This might be because of higher order effects in the calculation of the polarizabilities, which depend on the true shape of the object. Simulations with shear components γ_1 show similar results, although the error bars for the smallest objects are larger, because of undersampling.

Having shown that both the anisotropy and seeing correction work well independently, we now show the results of a simulation with an anisotropic PSF, with a position angle 90° away from the direction of the applied shear. As an additional test, we added a fair amount of noise to the data.

In Figure 21 we show the results of this simulation. One sees that the correction in this case is very large for small objects. Figure 21*b* shows the results when we calculate the "preseeing" shear polarizability using the procedure we advocate but in the absence of noise. The results in Figure 21*c* show that noise does not introduce a significant bias, although the errors for the smallest objects becomes very large. The shear from the smallest objects is underestimated slightly, because of the fact that the polarizabilities are calculated using an uncorrected value for the polarization. For small corrections this is a minor effect, but the correction needed in the simulation shown in Figure 21 is fairly large. In principle, one could improve the results by correcting the polarizabilities for this effect.

Although the shear might be biased low for the smallest objects, we feel that we can reliably recover the shear for objects with a scale length r_g larger than 1.2 pixels.

APPENDIX D

ANALYTIC RESULTS

As an analytic check on the simulations, we have calculated the polarizabilities and polarizations for the case when the PSF and the galaxy image are each the sums of two Gaussians. We have focused on the (in any case dominant) diagonal terms of the polarizabilities by considering only shears and polarizations in the e_1 component (the results for e_2 follow by symmetry upon rotating the axes by 45°). Thus we only consider Gaussians with principal axes aligned with the (x, y) coordinates.

As the PSF model, we take $[G(s_1, s_1 + \delta_1) + G(s_2, s_2 + \delta_2)]/2$, where $G(a, b)$ is a unit integral Gaussian $\exp[-x^2/(2a) - y^2/(2b)]/[2\pi(ab)^{1/2}]$ with x- and y-dispersions $a^{1/2}$ and $b^{1/2}$. The preseeing, preshearing galaxy image is assumed to be of the form $G(a_1, b_1) + G(a_2, b_2)$. It is then straightforward to calculate the axis lengths of this galaxy image after applying a shear γ: $a_i \to a_i' = a_i/(1 - \gamma)^2$ and $b_i \to b_i' = b_i/(1 + \gamma)^2$. Seeing convolution then turns this image into a sum of four Gaussians:

$$f = \sum_{ij} G(a_i' + s_j, b_i' + s_j + \delta_j)/2 \; . \tag{28}$$

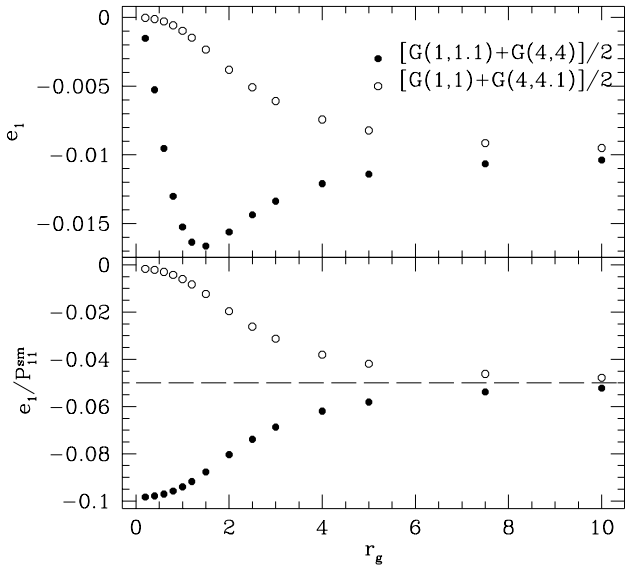

FIG. 22.—Measured polarization e_1 (*top*), obtained with a Gaussian weight function of dispersion r_g, and deduced estimate of the intrinsic polarization p_1 (*bottom*) for two double-Gaussian stellar profiles with identical second moments (and hence identical p_1). It is clear that the choice of weight function is important in the correction for PSF anisotropy.

While not completely general, these models already allow a large variety of PSF and galaxy shapes to be simulated: in particular, radially varying ellipticity profiles are possible. We have used symbolic mathematics to compute the polarizabilities and polarizations of the PSF and of the final observed image, assuming that the PSF anisotropy parameters δ_1 and δ_2 and the shear γ are small. A circular Gaussian weight function of dispersion r_g was used in these calculations.

First, we consider the measurement of the PSF anisotropy. In Figure 22 we compare the estimate e_1/P^{sm}_{11} of the PSF polarization for two PSFs with identical smear polarizability (to leading order in δ_i) and second moments but different ellipticity profiles. The plot shows that the choice of weight function is important: since the measured e_1 is different for the two models, it is impossible for the smear polarizability to correct both cases accurately. As may be seen, $|p_1|$ is systematically

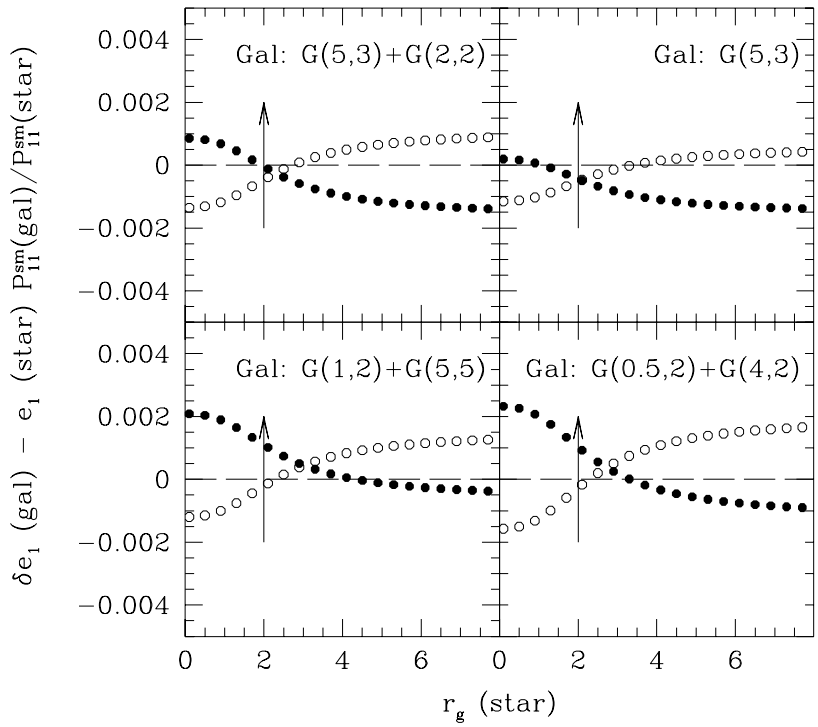

FIG. 23.—Simulations of the PSF anisotropy correction for double-Gaussian galaxies smeared with the two PSFs considered in Fig. 22. The galaxy image properties were measured with a Gaussian weight function of dispersion $r_g = 2$ (*vertical arrow*), and the stellar profiles were measured with r_g ranging from 0.1 to 8. The variances of the Gaussians making up the galaxy image are indicated in each panel: $G(a, b)$ stands for a unit-integral Gaussian of $\overline{x^2} = a$, $\overline{y^2} = b$. Circularly smeared galaxy polarizations are (*clockwise from top left*) 0.033, 0.068, −0.042, and −0.022. In each case, choosing a stellar r_g smaller than that used for measuring the galaxy image performs worse than when the stellar and galaxy r_g are similar.

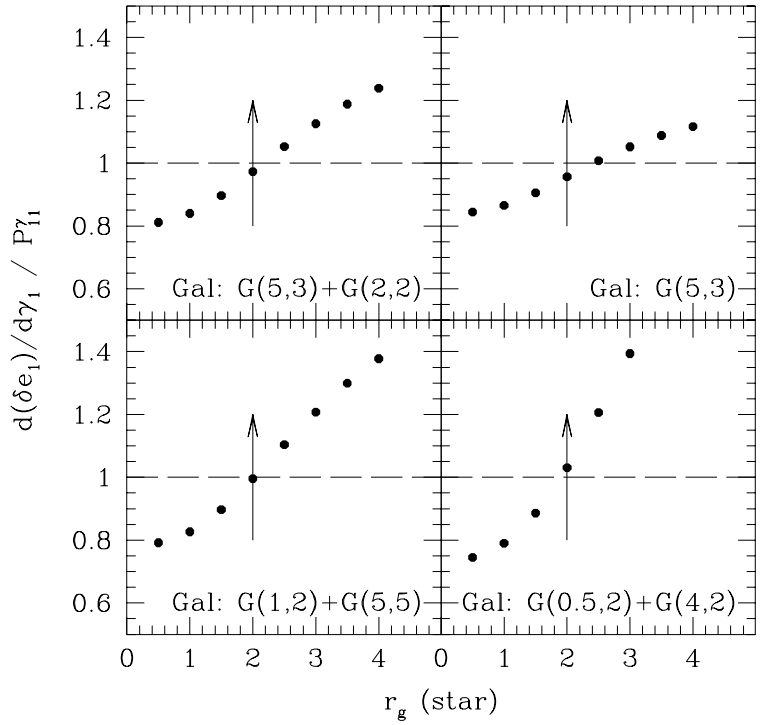

FIG. 24.—Simulations of the shear polarizability correction using the Luppino-Kaiser formalism. The given galaxy models are sheared by a (small) shear γ_1 and then smeared with the circular double-Gaussian PSF $[G(1, 1) + G(2, 2)]/2$. Then the Luppino-Kaiser preseeing shear polarizability P^{γ}_{11} is calculated using a Gaussian weight function of dispersion 2 (*arrows*) for the galaxy images and a range of dispersions r_g for the stellar PSF. The plot shows the ratio between the actual preseeing polarizability $d\delta e_1/d\gamma_1$ and the LK97 P^{γ}_{11}.

overestimated for a PSF with radially decreasing ellipticity.

What is the impact of these results on PSF anisotropy correction of galaxy polarizations? To answer this question, we have simulated the KSB95 procedure on an anisotropic double-Gaussian galaxy (see Fig. 23). We picked galaxy models with varying ellipticity profiles, convolved with the two PSFs considered above, and calculated the resulting polarization shifts δe_1 and smear polarizabilities $P^{\rm sm}_{11}$(gal) using a Gaussian weight function whose size matched the size of the galaxy image. This polarization shift was then corrected for PSF anisotropy following the KSB method, where when measuring the stellar images we allowed r_g(star) to vary. Evidently the correction depends on the stellar images' weight function, and a good compromise appears to be to take the stellar and the galaxy weight functions to be the same. Intuitively, this result is perhaps not surprising: it seems sensible to weigh the radial ellipticity profiles of a galaxy and the PSF in a similar fashion.

We have also examined the LK97 formalism for correcting for seeing convolution as a function of the size of the weight functions. Figure 24 shows the LK97 estimator $\delta e_1/P^{\gamma}_{11}$ for the shear, where again in $P^{\gamma} = P^{\rm sh}(\text{gal}) - P^{\rm sh}(\text{star})P^{\rm sm}(\text{gal})/P^{\rm sm}(\text{star})$ the stellar polarizabilities have been computed over a range of different r_g. Here large dependences on the stellar weight function are evident, and we conclude that the best strategy is to use the same Gaussian weight function for the stellar and for the galaxy images.

REFERENCES

Allen, S. W. 1998, MNRAS, 296, 392
Allen, S. W., & Fabian, A. C. 1994, MNRAS, 269, 409
Babul, A., & Ferguson, H. C. 1996, ApJ, 458, 100
Bartelmann, M., & Narayan, R. 1995, ApJ, 451, 60
Bautz, M., Honda, E., Ventrella, J., & Gendreau, K. 1997, in Proc. Int. Symp. on X-Ray Astron., X-Ray Imaging and Spectroscopy of Cosmic Hot Plasmas, ed. F. Makino & K. Mitsuda (Tokyo: Universal Acad. Press), 75
Blandford, R. D., Saust, A. B., Brainerd, T. G., & Villumsen, J. V. 1991, MNRAS, 251, 600
Bonnet, H., & Mellier, Y. 1995, A&A, 303, 331
Bonnet, H., Mellier, Y., & Fort, B. 1994, ApJ, 427, L83
Broadhurst, T. J., Taylor, A. N., & Peacock, J. A. 1995, ApJ, 438, 49
Bouwens, R., Broadhurst, T. J., & Silk, J. 1998, in preparation
Bouwens, R., & Silk, J. 1996, ApJL, 471, 19
Burstein, D., & Heiles, C. 1982, AJ, 87, 1165
Cardelli, J. A., Clayton, G. C., & Mathis, J. 1989, ApJ, 345, 245
Carlberg, R. G., Yee, H. K. C., & Ellingson, E. 1997, ApJ, 478, 462
Carlberg, R. G., Yee, H. K. C., Ellingson, E., Abraham, R., Gravel, P., Morris, S. M., & Pritchet, C. J. 1996, ApJ, 462, 32
Fahlman, G., Kaiser, N., Squires, G., & Woods, D. 1994, ApJ, 431, L71
Fischer, P., & Tyson, J. A. 1997, AJ, 114, 14
Fisher, D., Fabricant, D., Franx, M., & van Dokkum, P. G. 1998, ApJ, 498, 195
Fort, B., Mellier, Y., & Dantel-Fort, M. 1997, A&A, 321, 353
Franx, M., Illingworth, G. D., Kelson, D. D., van Dokkum, P. G., & Tran, K.-V. 1997, ApJ, 486, L75
Gronwall, C., & Koo, D. C. 1995, ApJ 440, L1
Holtzman, J. A., Burrows, C. J., Casertano, S., Hester, J. J., Trauger, J. T., Watson, A. M., & Worthey, G. 1995b, PASP, 107, 1065
Holtzman, J. A., et al. 1995a, PASP, 107, 156
Jørgensen, I. 1994, PASP, 106, 967
Kaiser, N., & Squires, G. 1993, ApJ, 404, 441
Kaiser, N., Squires, G., & Broadhurst, T. 1995a, ApJ, 449, 460 (KSB95)
Kaiser, N., Squires, G., Fahlman, G., & Woods, D. 1995b, Clusters of Galaxies, ed. F. Durret, A. Mazure, & J. T. T. Van (Gif-sur-Yvette: Editions Frontières)
Kelson, D. D, van Dokkum, P. G., Franx, M., Illingworth, G. D., & Fabricant, D. 1997, ApJ, 478, L13
Kormann, R., Schneider, P., & Bartelmann, M. 1994, A&A, 284, 285
Krist, J., & Hook, R. 1996, The Tiny Tim Users's Manual (Baltimore: StSci)

Lanzetta, K. M., Fernández-Soto, A., & Yahil, A. 1997, Proc. STSci. Symp. 1997 May, The Hubble Deep Field, ed. M. Livio, S. M. Fall, & P. Madau (Baltimore: STSci)
Lanzetta, K. M., Yahil, A., & Fernández-Soto, A. 1996, Nature, 381, 759
Le Fèvre, O., Hammer, F., Angonin, M. C., Gioia, I. M., & Luppino, G. A. 1994, ApJ, 422, L5
Luppino, G. A., Cooke, B. A., McHardy, I. M., & Ricker, G. R. 1991, ApJ, 102, 1
Luppino, G. A., & Kaiser, N. 1997, ApJ, 475, 20 (LK97)
Pozzetti, L., Bruzual, G. A., & Zamorani, G. 1996, MNRAS, 281, 953
Richer, H. B., et al. 1997, ApJ, 484, 741
Sawicki, M. J., Lin, H., & Yee, H. K. C. 1997, ApJ, 113, 1
Schneider, P. 1995, A&A, 302, 639
Schneider, P., & Bartelmann, M. 1996, MNRAS, 286, 696
Schneider, P., Ehlers, J., & Falco, E. E. 1992, Gravitational Lenses (Berlin: Springer)
Schneider, P., & Seitz, C. 1995, A&A, 294, 411
Seitz, C., Kneib, J.-P., Schneider, P., & Seitz, S. 1996, A&A, 314, 707
Seitz, C., & Schneider, P. 1995, A&A, 297, 287
Seitz, S., & Schneider, P. 1996, A&A, 305, 383
———. 1998, preprint (astro-ph/9802051)
Smail, I., Ellis, R. S., Dressler, A., Couch, W. J., Oemler, A., Jr., Sharples, R. M., & Butcher, H. 1997, ApJ, 497, 70
Smail, I., Ellis, R. S., Fitchett, M. J., & Edge, A. C. 1995, MNRAS, 273, 277
Squires, G., & Kaiser, N. 1996, ApJ, 473, 65
Squires, G., Kaiser, N., Babul, A., Fahlman, G., Woods, D., Neumann, D. M., & Böhringer, H. 1996a, ApJ, 461, 572
Squires, G., Kaiser, N., Fahlman, G., Babul, A., & Woods, D. 1996b, ApJ, 469, 73
Taylor, A. N., Dye, S., Broadhurst, T. J., Benitez, N., & van Kampen, E. 1998, preprint (astro-ph/9801158)
Tyson, J., Valdes, F., & Wenk, R. 1990, ApJ, 349, L1
van Dokkum, P. G., & Franx, M. 1996, MNRAS, 281, 985
van Dokkum, P. G., Franx, M, Kelson, D., Illingworth, D., Fisher, D., & Fabricant, D. 1998, ApJ, 500, 714
White, D. A., Jones, C., & Forman, W. 1998, MNRAS, 292, 419